Dopamine neurons projecting to the posterior striatum form an anatomically distinct subclass

William Menegas, Joseph F Bergan, Sachie K Ogawa, Yoh Isogai, Kannan Umadevi Venkataraju, Pavel Osten, Naoshige Uchida, Mitsuko Watabe-Uchida

DOI: http://dx.doi.org/10.7554/eLife.10032

Cite as: eLife 2015;10.7554/eLife.10032

Received: 11 July 2015
Accepted: 28 August 2015
Published: 31 August 2015

Dopamine neurons projecting to the posterior striatum form an anatomically distinct subclass

William Menegas[1], Joseph F. Bergan[1,2], Sachie K. Ogawa[1,3], Yoh Isogai[1], Kannan Umadevi Venkataraju[4], Pavel Osten[4], Naoshige Uchida[1], and Mitsuko Watabe-Uchida[1]

[1]Center for Brain Science, Department of Molecular and Cellular Biology, Harvard University, 16 Divinity Avenue, Cambridge, MA 02138, USA
[2]Present address: Department of Psychological and Brain Sciences, University of Massachusetts Amherst, 441 Tobin Hall, Amherst, MA 01003, USA
[3]Present address: RIKEN-MIT Center for Neural Circuit Genetics at the Picower Institute for Learning and Memory, Department of Biology and Department of Brain and Cognitive Sciences, Massachusetts Institute of Technology, 77 Massachusetts Avenue, Cambridge, MA 02139, USA
[4]Cold Spring Harbor Laboratory, 1 Bungtown Road, Cold Spring Harbor, NY 11724, USA

Correspondence: mitsuko@mcb.harvard.edu

Competing interests

Yoh Isogai and Joseph F. Bergan have filed a patent application on OptiView.

Abstract

Combining rabies-virus tracing, optical clearing (CLARITY), and whole-brain light-sheet imaging, we mapped the monosynaptic inputs to midbrain dopamine neurons projecting to different targets (different parts of the striatum, cortex, amygdala, etc.) in mice. We found that most populations of dopamine neurons receive a similar set of inputs rather than forming strong reciprocal connections with their target areas. A common feature among most populations of dopamine neurons was the existence of dense "clusters" of inputs within the ventral striatum. However, we found that dopamine neurons projecting to the posterior striatum were outliers, receiving relatively few inputs from the ventral striatum and instead receiving more inputs from the globus pallidus, subthalamic nucleus, and zona incerta. These results lay a foundation for understanding the input/output structure of the midbrain dopamine circuit and demonstrate that dopamine neurons projecting to the posterior striatum constitute a unique class of dopamine neurons regulated by different inputs.

Introduction

A longstanding challenge in neuroscience is to understand how neurons compute their output by integrating information from multiple sources. Mapping precise neural connectivity is a critical step towards understating neural computation. Recent developments in viral, molecular, and imaging techniques offer unprecedented opportunities to outline various aspects of the brain's wiring diagram in systematic and quantitative manners (Callaway and Luo, 2015; Denk et al., 2012; Hart et al., 2014; Huang and Zeng, 2013; Ogawa et al., 2014; Oh et al., 2014; Osten and Margrie, 2013; Pollak Dorocic et al., 2014; Watabe-Uchida et al., 2012; Weissbourd et al., 2014).

Midbrain dopamine neurons play important roles in various brain functions including motivation, reinforcement learning, and motor control (Ikemoto, 2007; Redgrave and Gurney, 2006; Schultz, 2007; Wise, 2004). Recording experiments have shown that many dopamine neurons signal reward prediction error (RPE): the discrepancy between predicted and actual reward value (Bayer and Glimcher, 2005; Bromberg-Martin et al., 2010; Clark et al., 2012; Cohen et al., 2012; Schultz, 2015; Schultz et al., 1997). Classically, it is thought that RPE coding is relatively uniform among dopamine neurons, and that dopamine's major function is to guide behavior toward maximizing future rewards. However, recent studies have suggested that there are at least two types of dopamine neurons, value-coding and salience-coding (Matsumoto and Hikosaka, 2008), although the extent of physiological diversity remains controversial (Fiorillo, 2013; Fiorillo et al., 2013a; Fiorillo et al., 2013b).

Most dopamine neurons reside in midbrain nuclei called the ventral tegmental area (VTA), the substantia nigra pars compacta (SNc), and the retrorubral field (RRF). Clusters of dopamine neurons in and around these nuclei are designated A10, A9, and A8, respectively. In the mouse brain, just ~30,000 dopamine neurons reside in these nuclei (Zaborszky and Vadasz, 2001). As with other monoamine neurotransmitters in the brain such as serotonin and noradrenaline, this small population of midbrain dopamine neurons exerts its influence over much of the brain as a neuromodulator. However, compared to the other monoamine neuromodulators, the dopamine system is anatomically unique in that the collateralization of dopamine neurons is limited (Moore and Bloom, 1978; Sobel and Corbett, 1984; Swanson, 1982). In other words, unlike the other monoaminergic neurons, a single dopamine neuron tends to target just one brain area, raising the possibility that different functional populations can be defined by the region that they target.

Recent studies have shown that dopamine neurons projecting to different targets have distinct properties (Kim et al., 2014; Lammel et al., 2008; Lammel et al., 2011; Lammel et al., 2014; Lammel et al., 2012). For instance, a population of dopamine neurons in the posterior medial VTA that projects to the medial prefrontal cortex (mPFC) in mice, is unique with respect to many features: low expression of dopamine transporter (DAT), tyrosine hydroxylase (TH), and the D2 dopamine receptor (D2R), narrow spike waveform, high baseline firing and low level of cocaine-induced synaptic plasticity (Lammel et al., 2008; Lammel et al., 2011; Lammel et al., 2014; Lammel et al., 2012). Dopamine neurons that project to different areas are located at slightly different, but highly overlapping locations in the midbrain (Swanson, 1982; Yetnikoff et al., 2014). These results have raised the possibility that projection target, rather than anatomical location, can better classify functional groups of dopamine neurons.

To understand how dopamine neurons compute their output, it is critical to know their inputs. Early systematic studies produced a thorough list of input areas to dopaminergic nuclei (Geisler et al., 2007; Geisler and Zahm, 2005) using conventional tracers. A recent study using a cell-type specific transsynaptic tracing method employing a rabies virus confirmed that many of these areas actually project directly onto dopamine neurons (Watabe-Uchida et al., 2012). This study also showed that VTA dopamine neurons received a distinct set of inputs compared to SNc dopamine neurons. It is possible that the differences observed in this study between inputs to VTA and SNc dopamine neurons were attributable to the uneven distribution of populations of dopamine neurons with different projection targets between these two nuclei. Both VTA and SNc contain dopamine neurons projecting to different targets, and each population of dopamine neurons projecting to a given target is distributed in a complex manner, often encompassing both VTA and SNc. Thus, it remains to be determined whether dopamine neurons projecting to different targets receive different or similar inputs.

In the present study, we classified dopamine neurons according to their projection targets and defined the distribution of monosynaptic inputs of each subpopulation. We compared the inputs of dopamine neurons defined by eight major targets: different parts of the striatum (ventral striatum [VS], dorsal striatum [DS], tail of the striatum [TS]), cortex (medial prefrontal cortex [mPFC], orbitofrontal cortex [OFC]), central amygdala (Amy), globus pallidus (GP), and lateral habenula (lHb). To collect and analyze this large data set, we developed a data acquisition and analysis pipeline using a brain clearing method (CLARITY) (Chung and Deisseroth, 2013), whole-brain imaging using light-sheet microscopy (Keller et al., 2010), and semi-automated

software for analysis. We found that populations of dopamine neurons projecting to most of these targets receive a similar set of inputs, while dopamine neurons projecting to TS ("tail of the striatum" or "posterior striatum") are a clear outlier. These results indicate that classifying dopamine neurons based on their projection target is a viable approach, and lay a foundation for studying the mechanisms by which dopamine neurons are regulated. Our approach is based on an automated imaging and analysis suite that will facilitate similar anatomical studies in other brain systems in an efficient and quantitative manner.

Results

Tracing monosynaptic inputs to projection-specific dopamine neurons

To visualize the monosynaptic inputs to dopamine neurons, we used a retrograde transsynaptic tracing system based on a modified rabies virus (SADΔG-EGFP(EnvA)) (Wickersham et al., 2007). This rabies virus is pseudotyped with an avian sarcoma and leukemia virus (ALSV-A) envelope protein (EnvA), so that the initial infection is restricted to cells that express a cognate receptor (TVA) in mammalian brains. In addition, this rabies virus lacks the gene encoding the rabies virus envelope glycoprotein (RG), which is required for trans-synaptic spread. This allows us to restrict trans-synaptic spread to cells that exogenously express RG. In this way, only monosynaptic (but not poly-synaptic) inputs are trans-synaptically labeled. In our previous work, we used two helper viruses to express TVA and RG under the control of Cre recombinase (AAV5-FLEX-TVA-mCherry and AAV8-FLEX-RG) (Watabe-Uchida et al., 2012). We previously injected these helper viruses into the VTA or SNc of transgenic mice expressing Cre specifically in dopamine neurons (dopamine transporter-Cre, or DAT-Cre) (Backman et al., 2006) to specifically label the monosynaptic inputs of these dopamine neurons throughout the brain (Watabe-Uchida et al., 2012).

In the present study, we sought to restrict the initial rabies infection to subpopulations of dopamine neurons defined by their projection sites. To do this, we injected a helper virus that expresses TVA under the control of Cre recombinase (AAV5-FLEX-TVA) into a dopamine projection site and co-injected a virus bearing blue fluorescent protein (AAV1-CA-BFP) to mark this site. Because it has been shown that minute TVA expression is sufficient for infection by ALSV-A (Belanger et al., 1995), we reasoned that DAT-Cre-expressing dopamine neurons in the

midbrain which were retrogradely infected by AAV5-FLEX-TVA would express enough TVA for initial rabies infection in a Cre-dependent manner (Figure 1A). To verify this, we injected AAV5-FLEX-TVA into one of the projection sites, the dorsal striatum (DS). After three weeks, rabies virus was injected into both VTA and SNc. In this experiment, we did not inject AAV8-FLEX-RG, so the rabies virus did not spread trans-synaptically. We did this to visualize only neurons that were directly infected by rabies virus (Figure 1B). Consistent with our intention, we observed that many VTA/SNc neurons were infected by the rabies virus and therefore expressed GFP (Figure 1B; Figure 1-figure supplement 1A). Based on antibody staining, almost all of the GFP-positive neurons were also positive for tyrosine hydroxylase (TH) (Figure 1C-F), a marker for dopamine neurons (98 ± 1%; n = 600 neurons, n = 3 mice). Given that injecting pseudotyped rabies virus alone resulted in very few infections (Watabe-Uchida et al., 2012), these results indicate that the injection of AAV5-FLEX-TVA into a dopamine projection site allowed us to restrict infection of rabies virus to dopamine neurons in a projection specific manner.

To allow rabies virus to spread trans-synaptically, we performed the same AAV5-FLEX-TVA injection to infect DS-projecting dopamine neurons, but this time also injected AAV8-FLEX-RG into both the VTA and SNc. Because a large quantity of RG is required for robust trans-synaptic spread, we injected this virus near the cell bodies of dopamine neurons (in the VTA and SNc) rather than near their axons. After three weeks, rabies virus was injected into both the VTA and SNc (Figure 1G). This resulted in a large number of trans-synaptically labeled GFP-positive neurons outside VTA/SNc (Figure 1H; Figure 1-figure supplement 1B). Together, these results demonstrate that our method allows us to label subpopulations of dopamine neurons defined by their projection sites and the monosynaptic inputs to these populations. We used this method to identify the monosynaptic inputs to dopamine neurons projecting to different targets.

Acquisition and analysis of rabies tracing data

Comparing the eight experimental groups required us to acquire and process a large data set. To achieve this goal, we developed a new data acquisition and analysis suite. In order to quantify the spread of rabies virus in each condition, we cleared brains using CLARITY to prepare them for light sheet microscopy (Figure 2A). Before imaging each brain, we pre-screened to ensure sufficient optical clarity by shining a 488nm light sheet through the ventral part of the brain and collecting light through an objective near the dorsal surface (~6mm away). Seventy-seven of 89 processed brains (~87%) were sufficiently clear for visualization of the ventral-most cells, and

only these brains were used. We imaged each brain from the dorsal and ventral sides (such that each image was a "horizontal" optical section), and then merged these images to create a continuous 3D image of the brain (Figure 2B).

Because rabies spreads to monosynaptic input neurons, the only information we ultimately needed to collect from each brain for the present goal of comparing the distribution of inputs was the position of each labeled cell body. Therefore, we only needed to image with sufficient resolution to distinguish every cell body throughout the brain (Figure 2C). This resulted in ~2Tb of image data from each brain, allowing us to image many brains, whereas imaging with even 2x higher magnification in each dimension would have led to prohibitively (based on our present processing capacity) large file sizes of ~20Tb per brain. We applied multiple segmentation algorithms to this data to classify each pixel as "cell" or "non-cell" (Figure 2D; see Materials and Methods). Quality of segmentation was consistent across many regions and imaging depths, including cortex (Figure 2E), striatum (Figure 2F), midbrain (Figure 2G), and cerebellum (Figure 2H). Because each cell was present in several images (at different depths), we then collapsed all neighboring "cell" pixels in all three dimensions to generate a list of the centroids of the detected cells. To compare the distribution of cells across brains, we aligned the autofluorescence image captured from each brain to a common "reference space" and used these transformations to align each set of centroids into this common space (see Materials and Methods). By aligning brains with different genetically defined populations of neurons labeled, we were able to determine the boundaries of major brain regions in this reference space in three dimensions. This strategy for analysis mirrors the analysis pipeline called "CUBIC", proposed for comparable analyses of whole-brain images acquired using a similar clearing method (Susaki et al., 2014).

Distribution of dopamine neurons projecting to different projection targets

The main target structure of midbrain dopamine neurons is the striatum. However, dopamine neurons also project to other brain areas including other basal ganglia structures, amygdala, and much of the cortex. We characterized the distribution of dopamine neurons that project to cortex (mPFC, OFC), striatum (VS, DS, TS), globus pallidus (GP), central amygdala (Amy) and lateral habenula (lHb). To do this, AAV5-FLEX-TVA was injected into one of the eight projection sites in DAT-Cre animals expressing Cre specifically in dopamine neurons (without injecting AAV8-FLEX-RG into the midbrain). Three weeks later, rabies virus was injected into both VTA and

SNc to infect dopamine neurons projecting to the area of the AAV5-FLEX-TVA injection (Figure 1A). Brain samples were collected after one week.

As previously reported, we found that dopamine neurons with distinct projection targets reside in different, but overlapping, areas of the midbrain (Figure 3; Figure 3-figure supplement 1; Figure 3-figure supplement 2; Figure 3-figure supplement 3) (Bjorklund and Dunnett, 2007; Haber, 2014; Lammel et al., 2008; Swanson, 1982). Interestingly, we observed an overlapping but dorso-laterally shifted distribution of dopamine neurons that project to VS, DS, and TS, in this order (Figure 3-figure supplement 1; Figure 3-figure supplement 2). Because many of the labeled populations of neurons overlapped in space, it is difficult to discriminate between populations based on location alone. In the case of Amy-projecting dopamine neurons, we observed labeling throughout VTA/SNc and also substantial labeling in supramammillary areas (A10rv) (Yetnikoff et al., 2014). In short, each brain area receives projections from dopamine neurons in slightly different, but highly overlapping subareas of VTA/SNc. Furthermore, we found that the distribution of labeled neurons in the VTA/SNc was similar in cases with and without transsynaptic spread (with and without RG, respectively), indicating that transsynaptic spread between primarily infected dopamine neurons and other dopamine neurons did not lead to the nonspecific infection of all dopamine neurons (Figure 3-figure supplement 3).

Distribution of inputs: TS-projecting dopamine neurons receive a unique set of inputs compared to other populations

Next, we mapped the monosynaptic inputs to these 8 subpopulations of dopamine neurons (Figure 3-figure supplement 4; Figure 3-figure supplement 5) defined by their projection target. Because the number of labeled neurons is different in each condition (Figure 1-figure supplement 1), comparing different conditions required a method of normalization. We first observed the distributions of labeled neurons by plotting the positions of labeled neurons for each condition. To normalize for the different numbers of total neurons labeled for visualization, we randomly sampled 1,500 neurons from each brain, and plotted corresponding neurons in coronal sections (Figure 3).

In our previous studies, we mapped the monosynaptic inputs to all of the dopamine neurons in VTA and SNc (Ogawa et al., 2014; Watabe-Uchida et al., 2012). We initially hypothesized that each of the eight populations would receive inputs from a subset of the regions identified in these

previous studies. Surprisingly, we found that the distribution of inputs to each population appeared to be largely similar (Figure 3). We found that monosynaptic inputs to most dopamine neurons were concentrated in the ventral striatum (Figure 3A) and that several areas containing inputs are continuous around the medial forebrain bundle, along the entire anterior-posterior axis (across the nucleus boundaries) (Figure 3A-E) as was observed previously (Geisler and Zahm, 2005; Watabe-Uchida et al., 2012), regardless of the projection targets. However, we found that TS-projecting dopamine neurons did not show a similar concentration of inputs: these neurons received many fewer inputs from anterior regions (Figure 3A, B) and ventromedial regions (Figure 3C, D). In short, these observations suggested that the overall distribution of inputs to TS-projecting dopamine neurons is different from those of the rest of the dopamine neuron populations (whose inputs largely overlapped with one another). We next examined these similarities and differences in more systematic and quantitative manners.

To quantify the differences between inputs to dopamine neurons with different projection sites, we compared the percentage of input neurons observed in each brain area in each condition (Figure 4). This normalization allowed us to average between brains within a given condition (n = 3-5 mice per condition, n = 4 for TS) and then to compare across conditions. Although we found some differences between subpopulations, the overall patterns were surprisingly similar. Among the brain systems, we found that the basal ganglia and hypothalamus provided the majority of inputs to dopamine neurons (Figure 4, Figure 4-figure supplement 1). In the basal ganglia, the ventral striatum (nucleus accumbens core and shell), dorsal striatum and ventral pallidum were the largest sources of inputs. In hypothalamus, the lateral hypothalamus (including the parasubthalamic nucleus) contained the largest number of inputs, and the preoptic areas also provided a substantial number. In the midbrain, the superior colliculus and dorsal raphe provided inputs as well.

In spite of similarities among dopamine populations, several prominent differences emerge upon focusing on TS-projecting dopamine neurons. While the ventral striatum is one of the largest sources of inputs to most of the subpopulations, it is a relatively minor source of inputs to TS-projecting dopamine neurons (Figure 3A, Figure 4). Instead, TS-projecting neurons receive an increased proportion of their inputs from the globus pallidus (GP, Figure 3C, Figure 4), entopeduncular nucleus (EP, Figure 3D, Figure 4), parasubthalamic nucleus (PSTh), subthalamic nucleus (STh) and zona incerta (ZI) (Figure 3E, Figure 4). To statistically verify these observations, we first performed a 1-way analysis of variance (ANOVA) among the 20 main

input areas (Figure 4-figure supplement 1). After correcting for multiple comparisons, nucleus accumbens shell, GP, STh and ZI remained significant ($p = 0.00045$, 0.0017, 0.00023, and 0.0028, respectively; significant after Holm-Sidak corrections for multiple comparisons). These differences are mainly attributable to the effect of the TS-projecting dopamine population. If we remove TS in the analysis, none of these areas retain statistical significance with the exception of the ventromedial hypothalamus ($p = 0.0028$, 1-way ANOVA), which appears to be a slightly larger source of inputs to VS-projecting dopamine neurons. Furthermore, in all of the above cases, the percentage of inputs from TS was significantly larger than the group mean of the remainder of the populations ($p < 0.001$; t-test). These results suggest that many dopamine neurons are embedded in a "canonical" circuit similar to VS-projecting dopamine neurons (which are known to encode reward prediction error), while TS-projecting dopamine neurons have a unique distribution of inputs and therefore form a distinct class of dopamine neurons.

By carefully examining the data, we could also discern some trends among the "canonical" populations of dopamine neurons. For example, DS-projecting dopamine neurons received more inputs from the neocortex than other populations (Figure 4), while VS-projecting dopamine neurons received more inputs from the olfactory tubercle and other ventromedial structures such as the ventromedial hypothalamus (Figure 4). Furthermore, DS-projecting and OFC-projecting dopamine neurons appeared to receive more inputs from the dorsal-most part of the dorsal striatum (Figure 3B). In the posterior midbrain, all populations received inputs from the dorsal raphe, but lHb-projecting dopamine neurons received fewer inputs from nearby areas (Figure 3H). In addition, lHb-projecting dopamine neurons received fewer inputs from posterior midbrain regions such as the periaqueductal grey and gigantocellular reticular nuclei (Figure 4). By far, though, the most distinct outlier was the set of inputs to TS-projecting dopamine neurons. In all of the cases in which our data attained statistical significance across all populations after correction for multiple comparisons (ventral striatum, ventromedial hypothalamus, globus pallidus, zona incerta, and subthalamic nucleus), TS-projecting neurons were the clear outliers (Figure 4-figure supplement 1).

To further quantify the overall similarity of patterns of inputs between conditions, we calculated pair-wise correlations (Pearson's correlation coefficients) between the percentage of input neurons across anatomical areas (Figure 5). We found that most pairs had relatively high correlations ($r = 0.85$ - 0.98). Here again, TS-projecting dopamine neurons had consistently lower correlations than other populations (Figure 5A): TS-projecting dopamine neurons were

most distinct from VS- and DS-projecting dopamine neurons (r = 0.65 and 0.69, respectively) (Figure 5A), although the similarity was slightly higher compared to non-striatal regions (r = 0.69 – 0.82). Hierarchical clustering supported this view: TS-projecting dopamine neurons were an outlier among the populations tested (Figure 5B). Together, these results show that TS-projecting dopamine neurons receive the most unique set of inputs among the populations of dopamine neurons that we examined.

Inputs to TS-projecting dopamine neurons are dorso-laterally shifted compared to inputs to other populations of dopamine neurons

When parceling the data based on brain regions, we found that most dopamine neurons receive more inputs from structures along the ventral medial part of the basal ganglia and hypothalamus, while TS-projecting dopamine neurons receive more inputs from subthalamic areas. Because we noticed that labeled neurons often did not respect the boundaries between regions (i.e. they did not form discrete clusters corresponding to each sub-region) and that distributions of labeled neurons were not always uniform in each area (e.g. the lateral hypothalamus), we also examined the general topography of inputs in these areas irrespective of regional boundaries.

We found that, in several coronal planes along the A-P axis, the center of mass of labeled neurons differed between conditions. Interestingly, we observed that the inputs to TS-projecting dopamine neurons were shifted dorso-laterally compared to the inputs to other subpopulations (Figure 6). In the anterior part of the brain, this shift is caused by the relatively low number of inputs from the ventral striatum to TS-projecting dopamine neurons (Figure 6A). In the middle sections of the brain, the shift is caused by an increased number of inputs from globus pallidus (Figure 6B) and entopeduncular nucleus (Figure 6C), as well as a decrease in inputs from the ventromedial hypothalamus. Finally, in a more posterior section of the brain, this shift is caused by the large number of inputs from the subthalamic and parasubthalamic nuclei to TS-projecting neurons (Figure 6D), as well as the lower number of inputs from the ventromedial hypothalamus.

In summary, we found that the center of mass of inputs to TS-projecting dopamine neurons were dorso-laterally shifted compared to inputs to other subpopulations in several coronal planes (Figure 6E-H). This suggests that the input pattern to TS-projecting dopamine neurons was unique, regardless of the method used for analysis. Although the meaning of the shift is not clear,

overall, our analysis revealed that the inputs to subpopulations of dopamine neurons were topographically organized within and across nucleus boundaries.

TS-projecting dopamine neurons do not receive inputs from "clusters" within the VS that are common sources of inputs to other dopamine neurons

As we discussed above, the most prominent inputs to the "canonical" dopamine neurons are from the nucleus accumbens, a part of the ventral striatum, though TS-projecting dopamine neurons received far fewer inputs from the nucleus accumbens (Figure 3A, Figure 4, Figure 7A-D). For each of the "canonical" populations, between 12% and 20% of the input neurons were located in the ventral striatum whereas only 5% of the input neurons were located in the ventral striatum for TS-projecting dopamine neurons (Figure 7D).

Our labeling showed discrete peaks of high density within the nucleus accumbens that do not correspond to the boundaries of commonly delineated sub-areas of this region (i.e. "core" or "shell") (Figure 7E-H). Our previous study reported the existence of these "ventral patches" in consistent locations across animals (Watabe-Uchida et al., 2012). In the present study, using precise 3D density plotting, we determined the exact number and locations of these patches: 5 total, with 3 in the anterior medial ventral shell, 1 in the medial core and 1 in the posterior lateral shell (Figure 7G-H, Figure 7-figure supplement 1).

We observed these dense patches of inputs in all cases, with the exception of inputs to TS-projecting dopamine neurons (Figure 7A-C, J). Of the input neurons in the nucleus accumbens, 16-26% were localized to these patches for all of the "canonical" populations (Figure 7I). By contrast, the few inputs that TS-projecting neurons did receive from the nucleus accumbens were not concentrated in patches (Figure 7C, I, J). Thus, whereas neurons in the ventral patches may play a key role in regulation of dopamine neurons, TS-projecting dopamine neurons may be relatively disconnected from this regulatory system.

We next compared the distribution of inputs from these patches between different populations of dopamine neurons. We found that each subpopulation received inputs differentially from different patches. For example, mPFC-projecting dopamine neurons received a larger ratio of inputs from the most medial patch, while Amy-projecting dopamine neurons received more of their inputs from the lateral patches (Figure 7J). Each of these patches could potentially have a distinct

functional role, and their contributions to dopamine neurons should be considered individually in future experiments.

Reciprocity is not a defining characteristic of midbrain dopamine neuron circuitry

We observed that most populations of dopamine neurons receive a large number of monosynaptic inputs from the ventral striatum. Because dopamine neurons also innervate the ventral striatum, we wondered whether VS-projecting neurons receive a larger proportion of inputs from the VS than other populations and whether the other populations received a larger proportion of inputs from their respective projection sites. Because we labeled the AAV-FLEX-TVA virus injection sites with BFP (to label the areas that the infected dopamine neurons project to, in each case), monosynaptic inputs residing within the BFP-labeled regions are more likely to have reciprocal connections with dopamine neurons. Because the CLARITY-based clearing process completely degraded the native fluorescence of BFP, we sliced the brains into 1mm sections and stained them with an anti-BFP antibody to reveal the injection sites. We examined the distribution of inputs with respect to these injection sites. Surprisingly, we did not observe that monosynaptic inputs accumulated in BFP-labeled areas (Figure 8A-F).

To quantify this observation, we compared the number of potential reciprocal inputs to each subpopulation to the average number of inputs in this area among all other subpopulations. First, we compared how many inputs each population receives from the nucleus that it projects to. We found that there was some variability, but that no population received a statistically significantly higher fraction of inputs from the region that it projected to (Figure 8G). Because some of our injections were limited to a portion of a region (for example, our injection into the dorsal striatum only covered the anterior medial dorsal striatum), we did a further analysis using the injection sites instead of the targeted nuclei to quantify the data. With this analysis, we also found no statistically significant differences (Figure 8H). In short, we observed that reciprocal monosynaptic connections are not a defining characteristic of inputs to dopamine neurons with differing projection targets (Figure 9). Rather, we found that most dopamine neurons (besides TS-projecting dopamine neurons) have similar inputs regardless of their projection target.

Discussion

In this study, we mapped the monosynaptic inputs to subpopulations of dopamine neurons defined by their projection targets. Our data show that reciprocal connectivity with target areas is not a prominent feature of dopamine neurons. Instead, most populations of dopamine neurons receive a surprisingly similar set of inputs. On the other hand, we found a systematic outlier: dopamine neurons projecting to the tail of the striatum receive a distinct set of inputs compared to dopamine neurons projecting to other targets. This conclusion was supported by the following observations. First, when the percent of inputs from a given area was found significantly different among conditions (1-way ANOVA), TS-projecting dopamine neurons were the main driver of these differences. TS-projecting dopamine neurons received far fewer inputs from the nucleus accumbens, whereas TS-projecting neurons received uniquely higher numbers of inputs from the globus pallidus (GP), subthalamic nucleus (STh), and zona incerta (ZI). Second, our examination of the spatial shift of input neurons in coronal optical sections also indicated that the center of mass of inputs to the TS-projecting population tended to be located more lateral and dorsal while the center of mass of inputs for the VS-projecting population tended towards the opposite. Third, correlation analysis and hierarchical clustering indicated that the pattern of inputs to TS-projecting dopamine neurons was most distinct from other conditions. Together, these results indicate that the dopamine neurons projecting to the posterior striatum form a distinct class of dopamine neurons.

The basic architecture of the dopamine circuit

The brain performs complicated tasks using layers of hierarchical and/or parallel neural circuits. Alheid and Heimer proposed that a major organizational principle of the brain is the existence of parallel functional and anatomical macrosystems, each comprised of a cortical area, a cortical input nucleus (such as an area in the striatum), an output nucleus (such as a part of the pallidum), thalamus, and brainstem (Alheid and Heimer, 1988; Zahm, 2006). According to this view, each macrosystem (such as the ventral striatum, the dorsal striatum, or the extended amygdala) would have its own dedicated dopamine system, resulting in a circuit organization resembling many parallel closed loops. This idea is plausible, considering the topographical organization of the dopaminergic nuclei (Swanson, 1982; Yetnikoff et al., 2014), and it could explain the diverse function of dopamine neurons. If dopamine neurons encode RPE, each macrosystem could learn independently through its own feedback. To test this directly, we asked whether dopamine neurons projecting to a nucleus in one macrosystem receive a larger proportion of their inputs from that nucleus or from other nuclei in that same macrosystem.

In stark contrast to this proposal, we found only loose reciprocity between dopamine neurons and their projection targets. If RPE is used to correct a neuron's behavior so that the neuron could represent predicted value more accurately in the future, a logical structure could be for prediction (expectation) to be sent to dopamine neurons and then for the same dopamine neurons to send back the error of the prediction (RPE) to the same neuron or the same system. Although many areas that receive dopamine projections also send projections to dopamine neurons, we found that reciprocal connections are not a basic principle explaining the distribution of monosynaptic inputs. In other words, reciprocal connectivity might not be the general mechanism of RPE computation and dopamine functions. Our data suggests that neurons in cortex, striatum, pallidum, habenula, or amygdala may not "entrain" different populations of dopamine neurons. Rather, most dopamine neurons are more likely to gather information from a set of common sources and broadcast a common RPE to many brain areas (Figure 9), while specific populations with different sets of inputs, such as TS-projecting dopamine neurons, might have different functions.

Previously, we found that many brain regions send monosynaptic inputs to dopamine neurons (Watabe-Uchida et al., 2012). However, which of these brain areas are most important for RPE computation remains unclear. Because the ventral striatum was reported to receive a RPE signal from dopamine neurons (Clark et al., 2012; Hart et al., 2014; Roitman et al., 2008), we reasoned that finding the monosynaptic inputs to VS-projecting dopamine neurons would narrow down the list of inputs that are potentially important to RPE computation. Although we were able to rule out some of the areas mentioned above which preferentially project to TS-projecting dopamine neurons, many brain areas still remain on the list of prominent inputs to VS-projecting dopamine neurons. Based on this logic, many brain areas have the potential to directly modulate RPE in dopamine neurons.

The tail of the striatum

Our results suggest that dopamine neurons projecting to the anterior versus posterior part of the striatum receive distinct inputs. Considering that dopamine plays essential roles in striatal functions, this result provides insight into the functioning of different parts of the striatum. Most commonly, the striatum is divided into two parts along the dorso-ventral axis: ventral striatum (or nucleus accumbens in rodents, also called the "limbic" striatum) and dorsal striatum. In addition,

the striatum is divided into more sub-regions by splitting the ventral striatum into "core" and "shell" regions and splitting the dorsal striatum into dorso-medial (associative) and dorso-lateral (motor-related) regions (Francois et al., 1994; Haber et al., 2000; Joel and Weiner, 2000; Lynd-Balta and Haber, 1994; Redgrave et al., 2010). In primates, projections from different cortical areas define different striatal regions. Projections from dorsolateral prefrontal cortex (DLPFC) and pre-supplementary motor cortex preferentially target associative striatum, whereas projections from orbitofrontal cortex (OFC) are unique to the limbic striatum. In rodents, there is a substantial controversy over the existence and location of homologous structures to the DLPFC or OFC of the monkey (Kita et al., 2014; Preuss, 1995; Uylings et al., 2003; Vertes, 2004). Thus, it is difficult to define the subareas of the striatum in the mouse brain. Nonetheless, even if it is not perfectly homologous to the primate striatum, previous studies suggest that the rodent striatum could contain a functional gradient from ventromedial to dorsolateral in agreement with the organization of cortical projections (Berendse et al., 1992; Voorn et al., 2004).

The three regions of the striatum that we targeted for investigation, VS, DS, and TS may reside roughly in this order in this gradient (Figure 3-figure supplement 5). Our target for DS (or the dorsal head) belongs to the "dorso-medial" subarea, whereas TS (or the posterior striatum) consists of proportionally a more "dorso-lateral" portion with some "dorso-medial" and "ventral" portions. Supporting the notion that these populations form a functional gradient, the input patterns to TS-projecting dopamine neurons are slightly more similar to that of DS-projecting dopamine than VS-projecting dopamine (Figure 8). However, we found that the similarity of inputs between DS- and VS- projecting dopamine neurons was much higher than similarity of inputs between DS- and TS- projecting dopamine neurons. This could potentially be explained by the fact that our injections into DS and VS were much closer together along the A-P axis (Figure 3-figure supplement 5). It may be fruitful to investigate a potential functional gradient along the A-P axis of the striatum in the future.

Previous studies suggested that there is a functional difference between anterior and posterior striatum in monkey and human (Lehericy et al., 2005; Miyachi et al., 1997). For example, it has been shown that the anterior striatum is important for skill learning and the posterior part is important for skill execution in monkeys (Miyachi et al., 1997). More recently, Kim and Hikosaka showed that the anterior caudate encodes flexible values, whereas the posterior caudate encodes stable values (Kim and Hikosaka, 2013). It would be interesting to determine whether this type of specialization for flexible or stable value coding applies also to the anterior and

posterior parts of the putamen. It also remains unknown whether the striatum in rodents contains similar functional differences between the anterior and posterior parts.

Increasing evidence suggests that dopamine neurons projecting to the ventral striatum signal RPE (Clark et al., 2012; Hart et al., 2014; Roitman et al., 2008), however, it remains to be clarified whether dopamine neurons projecting to other brain areas send distinct signals. Our results raise the possibility that dopamine neurons projecting to the tail of the striatum convey a different type of information than RPE. One interesting possibility is that dopamine signals in the tail of the striatum lack mechanisms to update the value representation based on the consequences of actions, consistent with the idea that the dopamine recipient neurons residing in this part of the striatum store "stable values" (Kim and Hikosaka, 2013). Dopamine is involved in different aspects of reward-based learning (e.g. goal-directed versus habit) as well as a wider range of functions besides reward-based learning, including motor and cognitive functions. It is therefore possible that TS-projecting dopamine neurons are related to habitual behavior or one of these other functions, unlike other dopamine neurons that signal RPE.

Unique set of monosynaptic inputs to TS-projecting dopamine neurons

The most prominent feature of TS-projecting dopamine neurons is that there are many fewer inputs from the ventral striatum (especially from the ventral patches), whereas the ventral striatum is one of the largest sources of inputs to the other dopamine neurons we investigated. Various models of RPE computations assume specific roles for inputs from particular areas. For instance, it has often been assumed that the striatum sends inhibitory "expectation" signals to dopamine neurons that can "cancel out" reward values when they are expected (Doya, 2008; Houk and Adams, 1995; Khamassi and Humphries, 2012; Kobayashi and Okada, 2007; Rao, 2010). Our finding that most populations of dopamine neurons received heavy innervation from the ventral striatum, which might encode "expectation" or "state values" in a RPE calculation, suggest that dopamine signals in these target areas are suppressed when reward is expected. On the other hand, our results indicate that TS-projecting dopamine neurons may not be subject to this type of regulation.

Rather than the ventral striatum, TS-projecting dopamine neurons received more inputs from the subthalamic nucleus (STh), parasubthalamic nucleus (PSTh), and zona incerta (ZI). STh is known for its role in motor function and is a uniquely glutamatergic structure of the basal ganglia

(whereas all the other nuclei in basal ganglia are mainly inhibitory). STh receives a strong projection from the globus pallidus (GP) in addition to the cortex (Canteras et al., 1990; Francois et al., 2004; Kita et al., 2014) and sends projections to other basal ganglia nuclei, such as striatum, GP, EP and SNr (Degos et al., 2008; Kita and Kitai, 1987). Interestingly, TS-projecting dopamine neurons receive inputs from STh as well as from areas that tend to be heavily interconnected with STh, such as GP, EP and SNr. These results suggest that, instead of inhibitory inputs from the ventral striatum ("direct pathway"), TS-projecting dopamine neurons receive more glutamatergic inputs from the STh ("hyperdirect pathway"), inhibitory inputs from pallidum ("indirect pathway"), and also inputs from two output nuclei: SNr and EP (Figure 9). Thus, cortical information may be transmitted to TS-projecting dopamine neurons through different pathways than other dopamine neurons. Finally, ZI, which is related to arousal, and PSTh, which is related to autonomic function, (Goto and Swanson, 2004; Kita et al., 2014), are additional unique pathways from cortex to TS-projecting dopamine neurons.

Ventral patches

Previous studies have shown that there are functional and histological subdivisions of the ventral striatum (Pennartz et al., 1994; Zahm and Brog, 1992). However, to our knowledge, there is no clear structure or function corresponding to the ventral patches that we described. In a previous study, we found that calbindin, a marker for patches in the dorsal striatum, partially distinguished the ventral patches from surrounding areas (Watabe-Uchida et al., 2012). These patches are, in essence, dense "hot spots" for inhibitory inputs to dopamine neurons whereas neurons outside the patches are predominantly indirectly (if at all) connected to dopamine neurons. One interesting possibility is that these ventral patches are negatively or positively correlated with the observation of "hedonic hot spots" within the striatum. These hot spots are so named because the "hedonic" desire for food was enhanced by the local stimulation of μ-opioid receptors residing in the medial-dorsal part of the anterior ventral striatum but not by the stimulation of neighboring areas (Castro and Berridge, 2014). Overall, the type of information each part of the striatum relays to dopamine neurons is an open question. Our anatomical definition of the stereotypical locations of the ventral patches will help guide future studies of what information is channeled through these microdomains (ventral patches) of the ventral striatum.

Relationship to Parkinson's disease

In Parkinson's disease, dopamine neurons in the SNc are progressively lost as the disease worsens. In particular, there is a prominent loss of dopaminergic axons in the posterior putamen and a corresponding loss of dopamine neurons in the ventrolateral SNc (Damier et al., 1999; Fearnley and Lees, 1991; Frost et al., 1993; Kish et al., 1988; Morrish et al., 1995; Pavese and Brooks, 2009; Redgrave et al., 2010). Interestingly, dopamine neurons projecting to the tail of the striatum preferentially reside in the lateral part of SNc, suggesting that the tail of the striatum in mice may be homologous to the posterior putamen.

One prominent feature of TS-projecting dopamine neurons is relatively strong input from STh. STh is uniquely excitatory compared to the other nuclei of the basal ganglia. Although the etiology of Parkinson's disease remains unclear, it has been proposed that uncontrolled, excessive excitation may eventually kill dopamine neurons (Olanow and Tatton, 1999; Rodriguez et al., 1998). The strong monosynaptic excitation from STh could at least partially explain why dopamine neurons that project to the posterior putamen are specifically vulnerable.

Because of the side effects of systemic L-DOPA administration, more and more patients have been receiving deep brain stimulation (DBS) as a treatment for Parkinson's disease (Benabid et al., 2009; Chaudhuri and Odin, 2010; Cyron et al., 2010; Deniau et al., 2010; Ponce and Lozano, 2010). Currently, the main targets for deep brain stimulation are STh, ZI, GPi (also called EP in rodents) and PPTg. Interestingly, our results showed that TS-projecting dopamine neurons receive monosynaptic inputs preferentially from all of these areas. In other words, effective DBS sites might reside in presynaptic sites that preferentially target TS-projecting dopamine neurons, rather than common inputs to all the dopamine neurons such as lateral hypothalamus (LH). As a result, DBS applied to these areas might influence only the circuits relevant to the TS-projecting dopamine system (most of which is lost in patients) without changing other aspects of dopamine functions, such as learning and reward-seeking behaviors. If this is true, the list of monosynaptic inputs to TS-projecting dopamine neurons will be a useful reference for seeking new DBS targets. Furthermore, expanding the framework for understanding the mechanism of DBS function could help improve its efficiency.

Technical considerations and relation with recent studies

In this study, we examined dopamine subpopulations that project to 8 different projection targets. Two studies were published very recently that are highly related to our present work. One study

found that monosynaptic inputs to dopamine neurons in VTA that project to medial and lateral NAc, mPFC and Amy were similar in all the areas they examined, with the exception of inputs from the dorsal raphe and within NAc (Beier et al., 2015). Similarly, another study found that monosynaptic inputs to neurons in SNc that project to medial DS and lateral DS were similar with the exception of inputs within DS (Lerner et al., 2015). Although neither of these studies examined TS-projecting dopamine neurons, the results are largely consistent with our finding that monosynaptic input patterns to most dopamine subpopulation are similar, and strengthen our finding that TS-projecting dopamine neurons are relatively unique. However, the patterns of inputs for VS-projecting neurons shown in the former study (Beier et al., 2015) and those for DS-projecting dopamine neurons in the latter study (Lerner et al., 2015) were quite different, in contrast to our finding. We previously observed different patterns of input between VTA and SNc dopamine neurons such as a strong preferential projection from DS to SNc (Watabe-Uchida et al., 2012). In the present study, we found that most populations of projection-specific dopamine neurons are distributed both in VTA and SNc. We, therefore, injected rabies virus both in VTA and SNc for all 8 conditions. The large difference in inputs between VS-projecting VTA neurons (Beier et al., 2015) and DS-projecting SNc populations (Lerner et al., 2015) may not be due to the difference in projection targets (VS versus DS), but rather because of the location of their virus injection sites (VTA versus SNc). It remains to be examined whether VTA dopamine neurons with a specific projection site receive a different set of monosynaptic inputs compared to SNc dopamine neurons that project to the same site (i.e. VTA->DS neurons versus SNc->DS neurons).

Our study relies on the assumption that each dopamine subpopulation defined by projection target is a different population. In general, dopamine axons from both VTA and SNc are mainly unbranched and thus target one structure (Fallon et al., 1978; Febvret et al., 1991; Matsuda et al., 2009; Sobel and Corbett, 1984; Swanson, 1982). However, there is some disagreement about the extent of collateralization of dopamine axons (Yetnikoff et al., 2014); some dopamine neurons may project to multiple brain areas (Fallon and Loughlin, 1982; Loughlin and Fallon, 1984; Takada and Hattori, 1986). Using CLARITY and whole brain imaging with membrane-bound GFP, Lerner et al. found that DS-projecting SNc neurons have negligible collateralization to NAc and no collateralization to other dopamine target areas such as prefrontal cortex or amygdala (Lerner et al., 2015). On the other hand, using conventional light microscope, Beier et al. found that lateral NAc-projecting dopamine neurons have broad arborizations going to DS, whereas medial NAc-projecting dopamine neurons do not project to the DS (Beier et al., 2015). They found that neither dopamine groups collateralize to mPFC or amygdala (Beier et al., 2015). In

spite of some discrepancies between studies, these studies show that dopamine neurons projecting to the target areas which we chose in the present study consist of largely non-overlapping subpopulations. However, because these studies could have overlooked sparse axon signals, we must interpret the results carefully, because any populations of dopamine neurons infected due to their projections to multiple areas would make the data appear more similar.

Our viral tracing method may allow trans-synaptic spread between dopamine neurons, which would make the trans-synaptically labeled populations appear more similar. However, the intrinsic connections in VTA/SNc originate mainly from non-dopamine neurons without TH immunoreactivity (Bayer and Pickel, 1990; Ferreira et al., 2008; Jhou et al., 2009). With respect to potential trans-synaptic spread, aforementioned studies overcame this problem by using CAV-Cre in wild type mice, sacrificing cell type specificity (Lerner et al., 2015) or by establishing a technically advanced method using CAV virus combined with Cre and Flp recombinase (Beier et al., 2015). Importantly, these studies also found that subpopulations of dopamine neurons had largely similar monosynaptic inputs.

We found that dopamine neurons that were infected with AAV5-FLEX-TVA at axon terminals provided sufficiently high levels of TVA to allow for subsequent infection with a modified rabies virus (i.e. SADΔG(envA)). This is a good reminder of the extremely high efficiency of this rabies tracing system and simultaneously reinforces its limitations: although some studies have used this system to examine inputs to ubiquitous cell types such as GABA neurons (Beier et al., 2015; Watabe-Uchida et al., 2012; Weissbourd et al., 2014), there is substantial risk for this AAV to infect not only Cre-expressing neurons in the injection site but also Cre-expressing neurons that project to that area, which may result in direct (i.e. non-transsynaptic) infections by the rabies virus. Proper controls are always necessary for tracing using this system, especially because a very small TVA infection could allow for subsequent rabies infection.

Automating whole brain rabies tracing

The acquisition and analysis of whole-brain tracing data has previously been accomplished by physically sectioning the brain at ~100 m intervals, imaging each (or every third) slice, manually defining regional boundaries in each section, and counting the number of cells in each region. This process is highly time-consuming and requires the dedicated attention of an expert in brain

anatomy. To acquire and analyze this type of data with higher throughput, we decided to make use of novel methods in imaging and analysis.

Several methods have recently been developed with the goal of acquiring an image of the whole mouse brain in an automated fashion. In broad terms, most strategies either employ serial sectioning 2-photon microscopy (Oh et al., 2014; Ragan et al., 2012) or optical clearing (Chung and Deisseroth, 2013) followed by light-sheet microscopy (Tomer et al., 2014). Serial sectioning 2-photon microscopy has the advantage of using an opaque brain as starting material, meaning that it doesn't require any clearing steps. Light-sheet imaging of cleared tissues, by contrast, allows for much more rapid image acquisition since there is no time spent physically sectioning the tissue and also because scanning is done with a sheet rather than a line. This increased scan speed allows for the rapid imaging of whole mouse brains with sufficient resolution to image every neuron. Because we wanted to characterize the distributions of all labeled neurons across brains, we decided to use light sheet microscopy on cleared brains.

Among methods to clear brains, a key distinction is between protocols that employ an inorganic solvent to reduce the internal differences in refractive index within a tissue and those that use an aqueous solution to wash away lipids and thereby reduce total scattering. Methods relying on inorganic solvents (such as iDISCO) denature native fluorescent proteins and require subsequent antibody staining (Renier and Tessier-Lavigne, 2014). Because we wanted to visualize GFP-labeled neurons, we decided to use CLARITY so that some native fluorescence (i.e. GFP and tdTomato) would remain intact, although we found that CLARITY causes a loss of mCherry and BFP fluorescence. Furthermore, exposure to inorganic solvents dramatically alters the size and overall morphology of the brain, while CLARITY leaves it relatively intact. Therefore, although the autofluorescence is dimmer in CLARITY-cleared brains (compared to iDISCO-cleared brains), brain structures are easier to identify. In summary, we found that the combination of CLARITY and light sheet microscopy allows for the rapid acquisition of whole brain rabies-tracing results.

Paired with automated cell detection and alignment between brains, this method allows for a consistent, unbiased, and automated analysis of tracing experiments that would previously have required countless hours of attention from an expert in brain anatomy.

Conclusions and Future Directions

Although the neural circuits controlling dopamine function are complex, a comprehensive understanding of the inputs/output structure of different populations of dopamine neurons will likely prove useful for understanding these circuits. In this study, we contributed to this effort in three different ways. First, we developed an automated pipeline for whole brain imaging, using a brain-clearing method (CLARITY), light sheet microscopy, and semi-automated data analysis. This will help to lower the hurdle for future systematic anatomy studies, and increase their consistency and efficiency. Second, we defined the full sets of monosynaptic inputs to eight subpopulations of dopamine neurons specified by projection targets. Third, we found that dopamine neurons projecting to the tail of the striatum are unique in their monosynaptic inputs, suggesting that they might also be an outlier functionally compared both to dopamine neurons projecting to other parts of the striatum and to those projecting to other brain regions (i.e. cortex, globus pallidus, amygdala). This foundational work also opens the door to further investigations. For example, what are the functional differences between the anterior and posterior (tail) regions of the striatum, and what is the role of dopamine in each? What information is calculated by dopamine neurons that project to different parts of the striatum, and how do the patterns of their inputs account for the differences in their signals? How is each dopamine population related to the symptoms of various disorders such as Parkinson's disease? We hope that our work will help guide these types of studies by providing them with a detailed circuit diagram as a starting point.

Materials and Methods

Animals

Eighty-nine male adult mice were used. These mice were the result of a cross with C57BL/6J mice and DAT (*Slc6a3*)-Cre mice such that they were heterozygous for Cre recombinase under the control of the dopamine active transporter (DAT) (Backman et al., 2006). Four male Vglut2 (*Slc17a6*)-Cre (Vong et al., 2011) crossed with B6.Cg-*Gt(ROSA)20Sor*$^{tm9(CAG\text{-}tdTomato)Hze}$/J (Jackson Laboratory) were used to help with the visualization of region boundaries. All procedures were in accordance with the National Institutes of Health Guide for the Care and Use of Laboratory Animals and approved by the Harvard Animal Care and Use Committee.

Viral Injections

pAAV-EF1 -FLEX-TVA was made by inserting TVA950 (Belanger et al., 1995) truncated after transmembrane domain in pAAV-EF1 -FLEX (Watabe-Uchida et al., 2012). pAAV-CA-BFP was made by cloning GFP with point mutations (BFP) (Subach et al., 2008) in pAAV-CA-FLEX-RG (Watabe-Uchida et al., 2012). AAVs were produced by the UNC Vector Core Facility.
In the first surgery, we injected 250-500 nl of adeno-associated virus (AAV) into the projection site (AAV5-FLEX-TVA, $1x10^{12}$ particles/ml and AAV1-BFP, $9x10^{12}$ particles/ml) and either AAV8-FLEX-RG ($2x10^{12}$ particles/ml) (Watabe-Uchida et al., 2012) (to label inputs), or no virus (to label only starter neurons) into both the VTA and SNc. After 3 weeks, in the second surgery, 250-500 nl of SADΔG-EGFP(EnvA) ($5x10^{7}$ plaque-forming units [pfu]/ml) (Wickersham et al., 2007) was separately injected into both the VTA and SNc. Brain samples were collected after one week. All surgeries were performed under aseptic conditions with animals anesthetized with isoflurane (1-2% at 0.5-1.0 L/min). Analgesia (ketoprofen, 5 mg/kg, I.P.; buprenorphine, 0.1 mg/kg, I.P.) was administered for the three days following each surgery. The virus injection sites are as follows: VTA) Bregma -3.1, Lateral 0.6, Depth 4.3 to 4.0, SNc) Bregma -3.1, Lateral 1.2, Depth 4.3 to 4.0, VS) Bregma 1.3, Lateral 0.5, Depth 3.8, DS) Bregma 1.0, Lateral 1.5, Depth 2.8, TS) Bregma -1.7, Lateral 3.0, Depth 2.35, mPFC) Bregma 2.1, Lateral 0.75, Depth 1.5, Angle 20 degrees, OFC) Bregma 2.45, Lateral 1.35, Depth 1.75, Amy) Bregma -1.35, Lateral 2.35, Depth 4.0, lHb) Bregma -1.8, Lateral 1.15, Depth 2.95, Angle 15 degrees, GP) Bregma -0.45, Lateral 1.85, Depth 3.5.

Perfusion in Hydrogel

To prepare a hydrogel solution, water, paraformaldehyde (PFA), phosphate buffered saline (PBS), Bis, and Acrylamide were mixed on ice, and then VA-044 Initiator (Fisher Scientific NC9952980) was added. Then, 50mL aliquots were made for storage at -20˚C. Hydrogel was thawed at -4˚C for 3 hours prior to each perfusion. During the perfusions, hydrogel solution was kept on ice. Immediately after the perfusions, brains were transferred to -4˚C. The recipe used for hydrogel:

40mL of 40% Acrylamide
10mL of 2% Bis
1 gram VA-044 Initiator
40mL of 10x PBS
100mL of 16% PFA
210mL of H_20

Oxygen/Nitrogen Exchange and Hydrogel Solidification

After 2 days of storage in hydrogel at 4˚C, oxygen was removed from tube using a food sealer and replaced with nitrogen. Immediately after oxygen/nitrogen exchange, tubes were placed in a water bath at 37˚C. After 1.5 hours, the hydrogel solution solidified into a jelly-like texture. At this point, brains were gently removed from the hydrogel using gloved fingers. Brains were placed on a paper (Kimwipe, Kimtech Science) and gently rolled over the paper so that excess hydrogel would come off of the brain. Great care was taken to ensure that all of the hydrogel was removed, but that none of the brain was damaged in the process. At this point, brains were put in PBST (0.1% Triton in PBS, pH=8) overnight at 37˚C on a rocker, covered by aluminum foil. After one day, brains were transferred to clearing solution. The recipe used for clearing solution:

123.66 g Boric Acid
400 g SDS
9.5 L H_2O
60 mL NaOH (10M)

Water, boric acid, and NaOH were mixed in a 5-gallon plastic container. Then, sodium dodecyl sulfate (SDS) was added 100g at a time while mixing. Finally, solution was left to mix for several hours on a rocker at 37˚C prior to use.

Tissue Clearing

Clearing was based on the original CLARITY protocol (Chung and Deisseroth, 2013). Simple and inexpensive parts were used in place of the originally proposed components. A Niagra 120V (Grey Beard 316) pump was used to circulate clearing solution. A KORAD Precision Adjustable 60V/5A (KA6005D) power supply was used to provide current at a constant voltage. A 5-gallon plastic container (US Plastic 97028) was used as a clearing solution reservoir and tubing was run though a second 5-gallon plastic container filled with water to cool the solution flowing through it. Chambers were constructed as previously described (Chung and Deisseroth, 2013) using a Nalgene chamber (Nalgene 2118-0002) and platinum wire (Sigma 267228). Clearing was done in a room held at 37˚C.

Electrophoresis was performed with a constant current of 30V, with an average temperature of 40˚C, over the course of 60 hours. With the voltage held at 30V, the current fluctuated between 0.5A and 1A, and generally stabilized at ~0.75A. The exact voltage/current relationship varied slightly depending on the chamber. The polarity of the electric field was switched every 12 hours. Clearing solution was replaced after every 120 hours of use (so, after using it twice). Platinum wire was replaced after every 1,200 hours of use (so, after using it twenty times). After removing brains from the clearing chamber and placing them in PBST (0.1% Triton, pH=8) for 24 hours, brains appeared snow white and expanded relative to their normal size.

Preparation for imaging

Brains were placed in an imaging solution called OptiView (Isogai, in press) (patent pending, application U.S. Serial No. 62/148,521) with refractive index 1.45 and pH 8 at room temperature on a rocker for 2 days before imaging. The imaging solution used was very similar to the recently described “RIMS” imaging solution (Yang et al., 2014). RIMS solution can be made as follows:

40 grams of Histodenz (Sigma)
30 mL PBS

NaOH to pH 7.5
RI to 1.46

Light-sheet imaging

Images were acquired with the Zeiss Z.1 Lightsheet microscope. Brains were glued to the tip of a 1 ml syringe (without needle) such that the posterior tip of the cerebellum was in contact with the syringe. Brains were then lowered into the imaging chamber. A 488nm laser was used to excite GFP and a 561nm laser was used to produce autofluorescence. Images were collected through a 5x objective with PCO-Edge scMOS 16 bit cameras with 1920 x 1920 pixels. Each frame was 2000 x 2000 μm, so each pixel was roughly 1.04 μm. The step size between images was set to 5.25 μm, so the voxels were not quite isotropic. Brains were imaged horizontally from the dorsal side, and then rotated 180 degrees for imaging from the ventral side. Each view was tiled with 7 x 6 tiles (14,000 x 12,000 μm) and the two views were combined to create a continuous image. Autofluorescence images were subsequently downsized to 700 x 600 x 350 pixels for alignment to the reference space. In these downsized images, voxels have 20 μm spacing in all 3 dimensions.

Cell Detection

Images were segmented into "cell" and "non-cell" pixels with 8 different segmentation algorithms. Each algorithm was trained with a selection of images from one of eight "parent regions" including: 1) olfactory bulb, 2) cortex/hippocampus, 3) thalamus, 4) striatum/pallidum, 5) hypothalamus, 6) midbrain, 7) hindbrain, and 8) cerebellum. For each of these parent regions, a random set of 50 images from 10 different brains were used to train each of the segmentation algorithms manually using Ilastik, software that has been recently applied to segment EM images (Maco et al., 2014; Sommer et al., 2011). Because neuron appearance and background fluorescence appearance differs drastically through the brain, segmentation algorithms only reliably recognized cells within the region they were trained on.

Ilastik was used to calculate 6 features for each pixel (Gaussian, Laplacian of Gaussian, Gaussian Gradient Magnitude, Difference of Gaussians, Structure Tensor Eigenvalues, Hessian of Gaussian Eigenvalues) with 3 radiuses (0.7 pixels, 1.6 pixels, and 5 pixels). In total, therefore, a vector with 18 values was produced for each pixel. During training, subsets of these vectors (pixels) would be

marked as “cell” or “non-cell” by a human in each of the training images and then the rest of the vectors’ identities were inferred using a random forest with 200 trees and 4 randomly chosen features per tree. Random sets of images from brains that were not part of the training set were used to manually verify the accuracy of segmentation.

After training, all 8 segmentation algorithms were applied to all of the images. This resulted in a binary version of the original data from the microscope with all pixels either classified as “1 (cell)” or “0 (non-cell)”. Because each cell was present in multiple Z positions, all sets of neighboring pixels that were labeled as “1 (cell)” pixels were collapsed in 3D using MATLAB to find the centroid of each detected cell. This afforded an extra opportunity to reduce noise by only counting “cells” that were within a reasonable range of diameters (2.5 m to 50 m), present in consecutive images, and with a reasonable shape (i.e. circularity of >0.1). Finally, the centroids’ positions were transformed into the reference space based on the result of autofluorescence alignment (see below). At this point, the centroids were masked using the outline of the appropriate parent region and combined. For example, only the results of the cortex segmentation algorithm within the cortex were retained.

Brain Alignment

The autofluorescence signals derived from 25 brains were averaged to produce a single “reference space” to serve as a template for subsequent brains. Subsequent brains were routinely aligned to this reference space using Elastix (Klein et al., 2010). We performed affine alignment followed by B-spline alignment based on mutual information, as previously proposed for human MRI image registration (Metz et al., 2011). The resulting transformation (from individual brain to reference space) was applied to the centroids of detected cells in order to plot all cells in the same reference space.

Atlas Construction

First, the 100 coronal slices of the Franklin and Paxinos atlas (Franklin and Paxinos, 2008) were manually aligned to the nearest matching optical slices of the reference brain (which has 700 coronal optical sections total). Then, boundaries of major regions were manually drawn onto each of these 100 slices. Finally, each region was manually smoothed in each dimension to produce continuous regions in 3D.

Immunohistochemistry

Brains were sectioned using a vibrotome with 1 mm spacing. After CLARITY, brains were extremely difficult to section owing to their unusual structural properties (soft, yet resistant to cutting). Slices were stained as previously described (Chung and Deisseroth, 2013). Briefly, primary antibody was applied at 1:200 for 2 days (then washed off for 1 day) and then secondary antibody was applied at 1:200 for 1 day (then washed off for 1 day). Every step (including washes) was performed at 37˚C on a rocker with PBST (0.1% Triton, pH=8) containing sodium borate (1M).

Confocal Imaging

After CLARITY, BFP signal was lost completely. An antibody (Evrogen #234, 1:100, Rabbit) was used to detect BFP signal and another (Abcam #76442, 1:100, Chicken) was used to detect TH. Brains were imaged to determine injection site and percentage of TH-positive starter cells using an inverted confocal microscope (Zeiss LSM 700). Stained 1 mm sections were placed in a glass-bottom well and then covered with a thin layer of imaging solution (as described above) to prevent them from drying during image acquisition. Images were acquired and stitched using Zeiss Blue.

Data analysis

Further data analysis was performed using custom software written in MATLAB (Mathworks, Natick, MA, USA). For statistical comparisons of the mean, we used 1-way analysis of variance (ANOVA) and the two-sample student's t-test, unless otherwise noted. The significance level was corrected for multiple comparisons using a Holm-Sidak method. All error bars in the figures are the standard error of the mean (s.e.m.).

To quantify the percentage of inputs, we excluded areas that contained dopamine cell bodies that could potentially have been starter cells in and around VTA, SNc, SNr and RRF, to avoid potential contamination from dopamine neurons in the counts of inputs. We defined the primary infection sites by adding the sites of all the dopamine cell bodies in experiments without RG (Figure 1A, Figure 3-supplement 1). We did not exclude A10rv in the supramammillary area

because DAT positive neurons in this area projected only to Amy and data did not change with or without this area.

To quantify the similarity in input patterns, we calculated Pearson's correlation coefficients between the percent of input neurons across anatomical areas. To compare spatial distributions of input neurons in the forebrain, the mean of the coordinates of all input neurons on a given coronal section was obtained. Hierarchical clustering was done using the correlation coefficients as a distance metric and using the average linkage function. Using other linkage functions produced similar results.

To define "ventral patches", we first pooled all neurons from all animals and plotted them in a reference space with 20μm x 20μm x 20μm voxels. A 3D Gaussian with kernel size of 60μm x 60μm x 60μm was then used to estimate the density of cells at each voxel. We defined ventral patches by finding the local maxima of the Gaussian-filtered 3D data and expanding stepwise pixel-by-pixel until either 1/3 of the maximum intensity or another patch boundary was reached.

Acknowledgements

We thank Ju Tian, Clara Starkweather, and other members of the Uchida lab and Dulac lab for helpful discussions. We are grateful to Drs. Linh Vong and Bradford Lowell for Vglut2-Cre mice. We also thank the staff of the Harvard FAS Research Computing Group as well as the staff of the Harvard Center for Biological Imaging for technical support.

References

Alheid, G.F., and Heimer, L. (1988). New perspectives in basal forebrain organization of special relevance for neuropsychiatric disorders: the striatopallidal, amygdaloid, and corticopetal components of substantia innominata. Neuroscience *27*, 1-39.

Backman, C.M., Malik, N., Zhang, Y., Shan, L., Grinberg, A., Hoffer, B.J., Westphal, H., and Tomac, A.C. (2006). Characterization of a mouse strain expressing Cre recombinase from the 3' untranslated region of the dopamine transporter locus. Genesis *44*, 383-390.

Bayer, H.M., and Glimcher, P.W. (2005). Midbrain dopamine neurons encode a quantitative reward prediction error signal. Neuron *47*, 129-141.

Bayer, V.E., and Pickel, V.M. (1990). Ultrastructural localization of tyrosine hydroxylase in the rat ventral tegmental area: relationship between immunolabeling density and neuronal associations. The Journal of neuroscience : the official journal of the Society for Neuroscience *10*, 2996-3013.

Beier, K.T., Steinberg, E.E., DeLoach, K.E., Xie, S., Miyamichi, K., Schwarz, L., Gao, X.J., Kremer, E.J., Malenka, R.C., and Luo, L. (2015). Circuit Architecture of VTA Dopamine Neurons Revealed by Systematic Input-Output Mapping. Cell *162*, 622-634.

Belanger, C., Zingler, K., and Young, J.A. (1995). Importance of cysteines in the LDLR-related domain of the subgroup A avian leukosis and sarcoma virus receptor for viral entry. Journal of virology *69*, 1019-1024.

Benabid, A.L., Chabardes, S., Mitrofanis, J., and Pollak, P. (2009). Deep brain stimulation of the subthalamic nucleus for the treatment of Parkinson's disease. The Lancet Neurology *8*, 67-81.

Berendse, H.W., Galis-de Graaf, Y., and Groenewegen, H.J. (1992). Topographical organization and relationship with ventral striatal compartments of prefrontal corticostriatal projections in the rat. The Journal of comparative neurology *316*, 314-347.

Bjorklund, A., and Dunnett, S.B. (2007). Dopamine neuron systems in the brain: an update. Trends in neurosciences *30*, 194-202.

Bromberg-Martin, E.S., Matsumoto, M., and Hikosaka, O. (2010). Dopamine in motivational control: rewarding, aversive, and alerting. Neuron *68*, 815-834.

Callaway, E.M., and Luo, L. (2015). Monosynaptic Circuit Tracing with Glycoprotein-Deleted Rabies Viruses. The Journal of neuroscience : the official journal of the Society for Neuroscience *35*, 8979-8985.

Canteras, N.S., Shammah-Lagnado, S.J., Silva, B.A., and Ricardo, J.A. (1990). Afferent connections of the subthalamic nucleus: a combined retrograde and anterograde horseradish peroxidase study in the rat. Brain research *513*, 43-59.

Castro, D.C., and Berridge, K.C. (2014). Advances in the neurobiological bases for food 'liking' versus 'wanting'. Physiology & behavior *136*, 22-30.

Chaudhuri, K.R., and Odin, P. (2010). The challenge of non-motor symptoms in Parkinson's disease. Progress in brain research *184*, 325-341.

Chung, K., and Deisseroth, K. (2013). CLARITY for mapping the nervous system. Nature methods *10*, 508-513.

Clark, J.J., Hollon, N.G., and Phillips, P.E. (2012). Pavlovian valuation systems in learning and decision making. Current opinion in neurobiology *22*, 1054-1061.

Cohen, J.Y., Haesler, S., Vong, L., Lowell, B.B., and Uchida, N. (2012). Neuron-type-specific signals for reward and punishment in the ventral tegmental area. Nature *482*, 85-88.

Cyron, D., Funk, M., Deletter, M.A., and Scheufler, K. (2010). Preserved cognition after deep brain stimulation (DBS) in the subthalamic area for Parkinson's disease: a case report. Acta neurochirurgica *152*, 2097-2100.

Damier, P., Hirsch, E.C., Agid, Y., and Graybiel, A.M. (1999). The substantia nigra of the human brain. II. Patterns of loss of dopamine-containing neurons in Parkinson's disease. Brain : a journal of neurology *122 (Pt 8)*, 1437-1448.

Degos, B., Deniau, J.M., Le Cam, J., Mailly, P., and Maurice, N. (2008). Evidence for a direct subthalamo-cortical loop circuit in the rat. The European journal of neuroscience *27*, 2599-2610.

Deniau, J.M., Degos, B., Bosch, C., and Maurice, N. (2010). Deep brain stimulation mechanisms: beyond the concept of local functional inhibition. The European journal of neuroscience *32*, 1080-1091.

Denk, W., Briggman, K.L., and Helmstaedter, M. (2012). Structural neurobiology: missing link to a mechanistic understanding of neural computation. Nature reviews Neuroscience *13*, 351-358.

Doya, K. (2008). Modulators of decision making. Nature neuroscience *11*, 410-416.

Fallon, J.H., and Loughlin, S.E. (1982). Monoamine innervation of the forebrain: collateralization. Brain research bulletin *9*, 295-307.

Fallon, J.H., Riley, J.N., and Moore, R.Y. (1978). Substantia nigra dopamine neurons: separate populations project to neostriatum and allocortex. Neuroscience letters *7*, 157-162.

Fearnley, J.M., and Lees, A.J. (1991). Ageing and Parkinson's disease: substantia nigra regional selectivity. Brain : a journal of neurology *114 (Pt 5)*, 2283-2301.

Febvret, A., Berger, B., Gaspar, P., and Verney, C. (1991). Further indication that distinct dopaminergic subsets project to the rat cerebral cortex: lack of colocalization with neurotensin in the superficial dopaminergic fields of the anterior cingulate, motor, retrosplenial and visual cortices. Brain research *547*, 37-52.

Ferreira, J.G., Del-Fava, F., Hasue, R.H., and Shammah-Lagnado, S.J. (2008). Organization of ventral tegmental area projections to the ventral tegmental area-nigral complex in the rat. Neuroscience *153*, 196-213.

Fiorillo, C.D. (2013). Two dimensions of value: dopamine neurons represent reward but not aversiveness. Science *341*, 546-549.

Fiorillo, C.D., Song, M.R., and Yun, S.R. (2013a). Multiphasic temporal dynamics in responses of midbrain dopamine neurons to appetitive and aversive stimuli. The Journal of neuroscience : the official journal of the Society for Neuroscience *33*, 4710-4725.

Fiorillo, C.D., Yun, S.R., and Song, M.R. (2013b). Diversity and homogeneity in responses of midbrain dopamine neurons. The Journal of neuroscience : the official journal of the Society for Neuroscience *33*, 4693-4709.

Francois, C., Grabli, D., McCairn, K., Jan, C., Karachi, C., Hirsch, E.C., Feger, J., and Tremblay, L. (2004). Behavioural disorders induced by external globus pallidus dysfunction in primates II. Anatomical study. Brain : a journal of neurology *127*, 2055-2070.

Francois, C., Yelnik, J., Percheron, G., and Fenelon, G. (1994). Topographic distribution of the axonal endings from the sensorimotor and associative striatum in the macaque pallidum and substantia nigra. Experimental brain research *102*, 305-318.

Franklin, B.J., and Paxinos, G. (2008). The mouse brain in stereotaxic coordinates. California: Academic.

Frost, J.J., Rosier, A.J., Reich, S.G., Smith, J.S., Ehlers, M.D., Snyder, S.H., Ravert, H.T., and Dannals, R.F. (1993). Positron emission tomographic imaging of the dopamine transporter with 11C-WIN 35,428 reveals marked declines in mild Parkinson's disease. Annals of neurology *34*, 423-431.

Geisler, S., Derst, C., Veh, R.W., and Zahm, D.S. (2007). Glutamatergic afferents of the ventral tegmental area in the rat. The Journal of neuroscience : the official journal of the Society for Neuroscience *27*, 5730-5743.

Geisler, S., and Zahm, D.S. (2005). Afferents of the ventral tegmental area in the rat-anatomical substratum for integrative functions. The Journal of comparative neurology *490*, 270-294.

Goto, M., and Swanson, L.W. (2004). Axonal projections from the parasubthalamic nucleus. The Journal of comparative neurology *469*, 581-607.

Haber, S.N. (2014). The place of dopamine in the cortico-basal ganglia circuit. Neuroscience *282C*, 248-257.
Haber, S.N., Fudge, J.L., and McFarland, N.R. (2000). Striatonigrostriatal pathways in primates form an ascending spiral from the shell to the dorsolateral striatum. The Journal of neuroscience : the official journal of the Society for Neuroscience *20*, 2369-2382.
Hart, A.S., Rutledge, R.B., Glimcher, P.W., and Phillips, P.E. (2014). Phasic dopamine release in the rat nucleus accumbens symmetrically encodes a reward prediction error term. The Journal of neuroscience : the official journal of the Society for Neuroscience *34*, 698-704.
Houk, J.C., and Adams, J.L. (1995). A Model of How the Basal Ganglia Generate and Use Neural Signals That. Models of information processing in the basal ganglia, 249.
Huang, Z.J., and Zeng, H. (2013). Genetic approaches to neural circuits in the mouse. Annual review of neuroscience *36*, 183-215.
Ikemoto, S. (2007). Dopamine reward circuitry: two projection systems from the ventral midbrain to the nucleus accumbens-olfactory tubercle complex. Brain research reviews *56*, 27-78.
Isogai, Y., Richardson, D., Dulac, C., and Bergan, J.F. (in press). Optimized protocol for imaging cleared neural issues using light microscopy. In Methods in Molecular Biology (Springer)
Jhou, T.C., Geisler, S., Marinelli, M., Degarmo, B.A., and Zahm, D.S. (2009). The mesopontine rostromedial tegmental nucleus: A structure targeted by the lateral habenula that projects to the ventral tegmental area of Tsai and substantia nigra compacta. The Journal of comparative neurology *513*, 566-596.
Joel, D., and Weiner, I. (2000). The connections of the dopaminergic system with the striatum in rats and primates: an analysis with respect to the functional and compartmental organization of the striatum. Neuroscience *96*, 451-474.
Keller, P.J., Schmidt, A.D., Santella, A., Khairy, K., Bao, Z., Wittbrodt, J., and Stelzer, E.H. (2010). Fast, high-contrast imaging of animal development with scanned light sheet-based structured-illumination microscopy. Nature methods *7*, 637-642.
Khamassi, M., and Humphries, M.D. (2012). Integrating cortico-limbic-basal ganglia architectures for learning model-based and model-free navigation strategies. Frontiers in behavioral neuroscience *6*, 79.
Kim, H.F., Ghazizadeh, A., and Hikosaka, O. (2014). Separate groups of dopamine neurons innervate caudate head and tail encoding flexible and stable value memories. Frontiers in neuroanatomy *8*, 120.
Kim, H.F., and Hikosaka, O. (2013). Distinct basal ganglia circuits controlling behaviors guided by flexible and stable values. Neuron *79*, 1001-1010.

Kish, S.J., Shannak, K., and Hornykiewicz, O. (1988). Uneven pattern of dopamine loss in the striatum of patients with idiopathic Parkinson's disease. Pathophysiologic and clinical implications. The New England journal of medicine *318*, 876-880.
Kita, H., and Kitai, S.T. (1987). Efferent projections of the subthalamic nucleus in the rat: light and electron microscopic analysis with the PHA-L method. The Journal of comparative neurology *260*, 435-452.
Kita, T., Osten, P., and Kita, H. (2014). Rat subthalamic nucleus and zona incerta share extensively overlapped representations of cortical functional territories. The Journal of comparative neurology *522*, 4043-4056.
Klein, S., Staring, M., Murphy, K., Viergever, M.A., and Pluim, J.P. (2010). elastix: a toolbox for intensity-based medical image registration. IEEE transactions on medical imaging *29*, 196-205.
Kobayashi, Y., and Okada, K. (2007). Reward prediction error computation in the pedunculopontine tegmental nucleus neurons. Annals of the New York Academy of Sciences *1104*, 310-323.
Lammel, S., Hetzel, A., Hackel, O., Jones, I., Liss, B., and Roeper, J. (2008). Unique properties of mesoprefrontal neurons within a dual mesocorticolimbic dopamine system. Neuron *57*, 760-773.
Lammel, S., Ion, D.I., Roeper, J., and Malenka, R.C. (2011). Projection-specific modulation of dopamine neuron synapses by aversive and rewarding stimuli. Neuron *70*, 855-862.
Lammel, S., Lim, B.K., and Malenka, R.C. (2014). Reward and aversion in a heterogeneous midbrain dopamine system. Neuropharmacology *76 Pt B*, 351-359.
Lammel, S., Lim, B.K., Ran, C., Huang, K.W., Betley, M.J., Tye, K.M., Deisseroth, K., and Malenka, R.C. (2012). Input-specific control of reward and aversion in the ventral tegmental area. Nature *491*, 212-217.
Lehericy, S., Benali, H., Van de Moortele, P.F., Pelegrini-Issac, M., Waechter, T., Ugurbil, K., and Doyon, J. (2005). Distinct basal ganglia territories are engaged in early and advanced motor sequence learning. Proceedings of the National Academy of Sciences of the United States of America *102*, 12566-12571.
Lerner, T.N., Shilyansky, C., Davidson, T.J., Evans, K.E., Beier, K.T., Zalocusky, K.A., Crow, A.K., Malenka, R.C., Luo, L., Tomer, R., *et al.* (2015). Intact-Brain Analyses Reveal Distinct Information Carried by SNc Dopamine Subcircuits. Cell *162*, 635-647.
Loughlin, S.E., and Fallon, J.H. (1984). Substantia nigra and ventral tegmental area projections to cortex: topography and collateralization. Neuroscience *11*, 425-435.

Lynd-Balta, E., and Haber, S.N. (1994). Primate striatonigral projections: a comparison of the sensorimotor-related striatum and the ventral striatum. The Journal of comparative neurology *345*, 562-578.

Maco, B., Cantoni, M., Holtmaat, A., Kreshuk, A., Hamprecht, F.A., and Knott, G.W. (2014). Semiautomated correlative 3D electron microscopy of in vivo-imaged axons and dendrites. Nature protocols *9*, 1354-1366.

Matsuda, W., Furuta, T., Nakamura, K.C., Hioki, H., Fujiyama, F., Arai, R., and Kaneko, T. (2009). Single nigrostriatal dopaminergic neurons form widely spread and highly dense axonal arborizations in the neostriatum. The Journal of neuroscience : the official journal of the Society for Neuroscience *29*, 444-453.

Metz, C.T., Klein, S., Schaap, M., van Walsum, T., and Niessen, W.J. (2011). Nonrigid registration of dynamic medical imaging data using nD + t B-splines and a groupwise optimization approach. Medical image analysis *15*, 238-249.

Miyachi, S., Hikosaka, O., Miyashita, K., Karadi, Z., and Rand, M.K. (1997). Differential roles of monkey striatum in learning of sequential hand movement. Experimental brain research *115*, 1-5.

Moore, R.Y., and Bloom, F.E. (1978). Central catecholamine neuron systems: anatomy and physiology of the dopamine systems. Annual review of neuroscience *1*, 129-169.

Morrish, P.K., Sawle, G.V., and Brooks, D.J. (1995). Clinical and [18F] dopa PET findings in early Parkinson's disease. Journal of neurology, neurosurgery, and psychiatry *59*, 597-600.

Ogawa, S.K., Cohen, J.Y., Hwang, D., Uchida, N., and Watabe-Uchida, M. (2014). Organization of monosynaptic inputs to the serotonin and dopamine neuromodulatory systems. Cell reports *8*, 1105-1118.

Oh, S.W., Harris, J.A., Ng, L., Winslow, B., Cain, N., Mihalas, S., Wang, Q., Lau, C., Kuan, L., Henry, A.M., *et al.* (2014). A mesoscale connectome of the mouse brain. Nature *508*, 207-214.

Olanow, C.W., and Tatton, W.G. (1999). Etiology and pathogenesis of Parkinson's disease. Annual review of neuroscience *22*, 123-144.

Osten, P., and Margrie, T.W. (2013). Mapping brain circuitry with a light microscope. Nature methods *10*, 515-523.

Pavese, N., and Brooks, D.J. (2009). Imaging neurodegeneration in Parkinson's disease. Biochimica et biophysica acta *1792*, 722-729.

Pennartz, C.M., Groenewegen, H.J., and Lopes da Silva, F.H. (1994). The nucleus accumbens as a complex of functionally distinct neuronal ensembles: an integration of behavioural, electrophysiological and anatomical data. Progress in neurobiology *42*, 719-761.

Pollak Dorocic, I., Furth, D., Xuan, Y., Johansson, Y., Pozzi, L., Silberberg, G., Carlen, M., and Meletis, K. (2014). A whole-brain atlas of inputs to serotonergic neurons of the dorsal and median raphe nuclei. Neuron *83*, 663-678.

Ponce, F.A., and Lozano, A.M. (2010). Deep brain stimulation state of the art and novel stimulation targets. Progress in brain research *184*, 311-324.

Preuss, T.M. (1995). Do rats have prefrontal cortex? The rose-woolsey-akert program reconsidered. Journal of cognitive neuroscience *7*, 1-24.

Ragan, T., Kadiri, L.R., Venkataraju, K.U., Bahlmann, K., Sutin, J., Taranda, J., Arganda-Carreras, I., Kim, Y., Seung, H.S., and Osten, P. (2012). Serial two-photon tomography for automated ex vivo mouse brain imaging. Nature methods *9*, 255-258.

Rao, R.P. (2010). Decision making under uncertainty: a neural model based on partially observable markov decision processes. Frontiers in computational neuroscience *4*, 146.

Redgrave, P., and Gurney, K. (2006). The short-latency dopamine signal: a role in discovering novel actions? Nature reviews Neuroscience *7*, 967-975.

Redgrave, P., Rodriguez, M., Smith, Y., Rodriguez-Oroz, M.C., Lehericy, S., Bergman, H., Agid, Y., DeLong, M.R., and Obeso, J.A. (2010). Goal-directed and habitual control in the basal ganglia: implications for Parkinson's disease. Nature reviews Neuroscience *11*, 760-772.

Rodriguez, M.C., Obeso, J.A., and Olanow, C.W. (1998). Subthalamic nucleus-mediated excitotoxicity in Parkinson's disease: a target for neuroprotection. Annals of neurology *44*, S175-188.

Roitman, M.F., Wheeler, R.A., Wightman, R.M., and Carelli, R.M. (2008). Real-time chemical responses in the nucleus accumbens differentiate rewarding and aversive stimuli. Nature neuroscience *11*, 1376-1377.

Schultz, W. (2007). Multiple dopamine functions at different time courses. Annual review of neuroscience *30*, 259-288.

Schultz, W. (2015). Neuronal Reward and Decision Signals: From Theories to Data. Physiological reviews *95*, 853-951.

Schultz, W., Dayan, P., and Montague, P.R. (1997). A neural substrate of prediction and reward. Science *275*, 1593-1599.

Sobel, E., and Corbett, D. (1984). Axonal branching of ventral tegmental and raphe projections to the frontal cortex in the rat. Neuroscience letters *48*, 121-125.

Sommer, C., Straehle, C., Koethe, U., and Hamprecht, F. (2011). ilastik: Interactive learning and segmentation toolkit. Paper presented at: Biomedical Imaging: From Nano to Macro, 2011 IEEE International Symposium on (IEEE).

Subach, O.M., Gundorov, I.S., Yoshimura, M., Subach, F.V., Zhang, J., Gruenwald, D., Souslova, E.A., Chudakov, D.M., and Verkhusha, V.V. (2008). Conversion of red fluorescent protein into a bright blue probe. Chemistry & biology *15*, 1116-1124.

Susaki, E.A., Tainaka, K., Perrin, D., Kishino, F., Tawara, T., Watanabe, T.M., Yokoyama, C., Onoe, H., Eguchi, M., Yamaguchi, S., *et al.* (2014). Whole-brain imaging with single-cell resolution using chemical cocktails and computational analysis. Cell *157*, 726-739.

Swanson, L.W. (1982). The projections of the ventral tegmental area and adjacent regions: a combined fluorescent retrograde tracer and immunofluorescence study in the rat. Brain research bulletin *9*, 321-353.

Takada, M., and Hattori, T. (1986). Collateral projections from the substantia nigra to the cingulate cortex and striatum in the rat. Brain research *380*, 331-335.

Tomer, R., Ye, L., Hsueh, B., and Deisseroth, K. (2014). Advanced CLARITY for rapid and high-resolution imaging of intact tissues. Nature protocols *9*, 1682-1697.

Uylings, H.B., Groenewegen, H.J., and Kolb, B. (2003). Do rats have a prefrontal cortex? Behavioural brain research *146*, 3-17.

Vertes, R.P. (2004). Differential projections of the infralimbic and prelimbic cortex in the rat. Synapse *51*, 32-58.

Vong, L., Ye, C., Yang, Z., Choi, B., Chua, S., Jr., and Lowell, B.B. (2011). Leptin action on GABAergic neurons prevents obesity and reduces inhibitory tone to POMC neurons. Neuron *71*, 142-154.

Voorn, P., Vanderschuren, L.J., Groenewegen, H.J., Robbins, T.W., and Pennartz, C.M. (2004). Putting a spin on the dorsal-ventral divide of the striatum. Trends in neurosciences *27*, 468-474.

Watabe-Uchida, M., Zhu, L., Ogawa, S.K., Vamanrao, A., and Uchida, N. (2012). Whole-brain mapping of direct inputs to midbrain dopamine neurons. Neuron *74*, 858-873.

Weissbourd, B., Ren, J., DeLoach, K.E., Guenthner, C.J., Miyamichi, K., and Luo, L. (2014). Presynaptic partners of dorsal raphe serotonergic and GABAergic neurons. Neuron *83*, 645-662.

Wickersham, I.R., Lyon, D.C., Barnard, R.J., Mori, T., Finke, S., Conzelmann, K.K., Young, J.A., and Callaway, E.M. (2007). Monosynaptic restriction of transsynaptic tracing from single, genetically targeted neurons. Neuron *53*, 639-647.

Wise, R.A. (2004). Dopamine, learning and motivation. Nature reviews Neuroscience *5*, 483-494.

Yang, B., Treweek, J.B., Kulkarni, R.P., Deverman, B.E., Chen, C.K., Lubeck, E., Shah, S., Cai, L., and Gradinaru, V. (2014). Single-cell phenotyping within transparent intact tissue through whole-body clearing. Cell *158*, 945-958.

Yetnikoff, L., Lavezzi, H.N., Reichard, R.A., and Zahm, D.S. (2014). An update on the connections of the ventral mesencephalic dopaminergic complex. Neuroscience *282C*, 23-48.
Zaborszky, L., and Vadasz, C. (2001). The midbrain dopaminergic system: anatomy and genetic variation in dopamine neuron number of inbred mouse strains. Behavior genetics *31*, 47-59.
Zahm, D.S. (2006). The evolving theory of basal forebrain functional-anatomical 'macrosystems'. Neuroscience and biobehavioral reviews *30*, 148-172.
Zahm, D.S., and Brog, J.S. (1992). On the significance of subterritories in the "accumbens" part of the rat ventral striatum. Neuroscience *50*, 751-767.

Figure 1: Labeling projection-specific dopamine neurons and their monosynaptic inputs throughout the brain with rabies-GFP

A) A schematic of the injections used to label projection-specific populations of dopamine neurons. The blue circle represents the site of infection with AAV-FLEX-TVA and green neurons represent the DAT-Cre-expressing dopamine neurons projecting to that area. **B)** Horizontal optical section showing rabies-GFP signal following AAV-FLEX-TVA injection into the striatum of a DAT-Cre animal followed by rabies injection into the VTA and SNc. Number of infected neurons shown in Figure 1 – figure supplement 1. Bar indicates 2 mm. **C)** Coronal physical section showing rabies labeled neurons from B) in green and anti-TH antibody staining in red. Bar indicates 500 μm. **D-F)** Higher magnification image of rabies labeled neurons and TH staining. Bars indicate 200 μm. **G)** A schematic of the injections used to label the inputs of projection-specific populations of dopamine neurons throughout the brain. The blue circle represents the site of infection with AAV-FLEX-TVA and the red circle represents the site of infection with AAV-FLEX-RG. Green neurons outside of VTA/SNc represent the monosynaptic inputs labeled throughout the brain. **H)** Horizontal optical section showing rabies-GFP signal following AAV-FLEX-TVA injection into the striatum and AAV-FLEX-RG into the VTA and SNc of a DAT-Cre animal followed by rabies injection into the VTA and SNc. Number of infected neurons shown in Figure 1 – figure supplement 1. Bar indicates 2 mm.

Figure 2: Automated acquisition and analysis of whole-brain tracing data

A) A schematic of the brain clearing, imaging, and analysis pipeline used to acquire data from brains labeled using the injection schematics outlined in Figure 1A and Figure 1G. **B)** A graphical explanation of the image acquisition and stitching process. Whole brains were imaged horizontally, from the dorsal (orange arrow) and ventral (purple arrow) sides and these images were stitched and combined to create a whole brain image. An example brain expressing tdTomato under the control of genetically encoded vglut2-Cre is shown. **C)** An example of a horizontal optical section acquired as described in A-B. Boxes indicate the locations of inset panels. Bar indicates 2 mm. **D)** The automatically generated segmentation of C, with each labeled cell being represented by a single pixel. Bar indicates 2 mm. **E-H)** Insets displaying raw images and automatically generated segmentations from the indicated regions (cortex, striatum, midbrain, and cerebellum). Bars indicate 200 μm.

Figure 3: Distribution of monosynaptic inputs to projection-specific populations of dopamine neurons throughout the brain

A summary of the inputs to each of the projection-specified populations of dopamine neurons assayed (using the injection scheme from Figure 1G) normalized such that the 1500 neurons were randomly sampled from each brain. We then combined such subsampled neurons from three randomly selected animals for each condition and plotted them in corresponding 400 um sections. Inputs to: VS-projecting, DS-projecting, TS-projecting, GP-projecting, Amy-projecting, OFC-projecting, mPFC-projecting, and lHb-projecting dopamine neurons as well as selected coronal sections for reference **(A-H)**. In this figure, and all others, the following abbreviations were used: "VS" for ventral striatum, "DS" for anterior dorsal striatum, "TS" for tail of the striatum (posterior dorsal striatum), "GP" for globus pallidus, "Amy" for amygdala, "OFC" for orbitofrontal cortex, "mPFC" for medial prefrontal cortex, and "lHb" for lateral habenula. Data collected in the same manner from experiments with no transsynaptic spread shown in Figure 3 – figure supplement 1 and Figure 3 – figure supplement 2, comparison of the two conditions shown in Figure 3 – figure supplement 3, and injection sites used shown in Figure 3 – figure supplement 4 and Figure 3-figure supplement 5. Bars indicate 2 mm.

Figure 4: Comparison of the percentage of inputs from each region across populations of projection-specific dopamine neurons

A summary of the distribution of inputs to dopamine neurons with different projection sites, with bars representing the average % of inputs observed (out of all labeled input neurons outside of the VTA/SNc/SNr/RRF) per region (mean ± s.e.m..). Each color represents inputs to a different population of dopamine neurons, as indicated in the inset. The 20 most prominent inputs are compared in Figure 4 – figure supplement 1.

Figure 5: Correlation between projection-specific populations of dopamine neurons

A) Scatter plots comparing the percent of inputs from each anatomical region for VS-, DS-, and TS-projecting dopamine neurons. Each circle represents the average percent of inputs for one anatomical area for each condition. *r*: Pearson's correlation coefficient. The axes are in log scale. **B)** Dendrogram (left) and correlation matrix (right) summarizing all pair-wise comparisons.

Color on the right indicates correlation values. The dendrogram was generated based on hierarchical clustering using the average linkage function.

Figure 6: Topological shift in the center of mass of input neurons to projection-specified dopamine neurons

Four coronal optical sections (400 μm thick) were chosen to demonstrate the dorsolateral shift of inputs to TS-projecting dopamine neurons. **A-D)** Coronal optical sections, with a region of interest marked in yellow for reference. Bars represent 2 mm. The distribution of inputs to each population of neurons is plotted in red and neurons within the ventral striatum **(A)**, globus pallidus **(B)**, entopeduncular nucleus **(C)**, and subthalamic nucleus **(D)** are indicated. A fixed number of neurons were randomly chosen from each brain and those neurons from three randomly chosen animals per condition were plotted for corresponding coronal sections. **E-H)** Coronal optical sections, with a yellow box showing the location of the insets displayed below. The center of mass for each population is shown, with vertical and horizontal lines representing the standard error in the y-axis and x-axis, respectively.

Figure 7: Dense regions of inputs within the ventral striatum

A-C) Coronal optical sections showing typical distributions of inputs in the ventral striatum. A comparison of the typical "patch" structure of inputs from the ventral striatum (to VS-projecting or DS-projecting dopamine neurons, for example) with the atypical "patch-less" structure of inputs from the striatum to TS-projecting dopamine neurons. **D)** Percentage of input neurons within the ventral striatum (core, medial shell, and lateral shell combined) in each condition. Red dotted line indicates the percentage expected based on chance distribution throughout the brain, while green dotted line indicates the average percentage among all animals. **E)** Horizontal optical section showing a typical distribution of inputs in the ventral striatum, with many input neurons in tight clusters. Bar represents 2 mm. **F)** A zoomed view of E, taken from the indicated box. Clusters are dispersed along the A-P axis, so two planes are used to display them in coronal sections: the black arrow indicates the anterior plane and the white arrow indicated the posterior plane. **G-H)** Coronal optical sections showing the two planes indicated above, as well as a graphical representation of the 5 patches in those planes. **I)** Among labeled neurons in the ventral striatum, the percentage within the patches in each condition. Red dotted line indicates the percentage expected based on chance distribution throughout the nucleus accumbens, while green

dotted line indicates the average percentage among all animals. **J)** Among labeled neurons within the patches, the percentages within each patch in each condition. Green arrows point to patch 2, cyan arrows point to patch 3, and yellow arrows point to patch 5. More detailed description of the patches shown in Figure 7 – figure supplement 1.

Figure 8: Reciprocity of connection between dopamine neurons and neurons at their projection sites

CLARITY-based brain clearing did not preserve native BFP fluorescence, so brains were physically sectioned and stained with an anti-BFP antibody to label the injection site of AAV-FLEX-TVA in each animal. **A-C)** The injection site (red) and input neurons (green) labeled in a physical coronal section for DS-projecting dopamine neurons. **D-F)** The injection site (red) and input neurons (green) labeled in a physical coronal section for VS-projecting dopamine neurons. **G)** A comparison of the percentage of inputs from the reciprocal region (defined by brain region) of each injection site (in purple) with the average percentage of inputs from that region among all other brains (in black). For this analysis, the dorsal striatum was split into "anterior dorsal striatum" for DS and "posterior dorsal striatum" for TS at Bregma -0.9 mm. There were no significant differences between pairs (two-sample t-test). **H)** A comparison of the percentage of inputs from the reciprocal site (defined by region of BFP infection) of each injection (in red) with the average percentage of inputs from that region among all other brains (in black). There were no significant differences between pairs (two-sample t-test).

Figure 9: Summary and Model

A) A working model suggesting that dopamine neurons receive inputs primarily from the region that they project to, based on the idea that input neurons provide an "expectation" signal and dopamine neurons correct them (i.e. send them a prediction error signal based on the type of expectation that they encoded) individually. **B)** Our model, in which dopamine neurons in the "canonical" pathway receive inputs primarily from a common set of regions (and particularly heavy inputs from the ventral striatum) and send a common prediction error signal to many parts of the forebrain. We propose that TS-projecting dopamine neurons could be part of a relatively separate pathway with a potentially unique function (different from reward prediction error calculation) based on its unique distribution of inputs. Some common inputs such as the dorsal striatum and ventral pallidum are omitted for clarity.

Figure supplements

Figure 1 – figure supplement 1: Number of starter cells and inputs labeled

A) The average numbers of projection-specified dopamine neurons labeled in each condition, using the injection schematic shown in Figure 1A with the indicated injection sites of AAV-FLEX-TVA on the x-axis of the graph. Mean ± s.e.m. **B)** The average numbers of inputs (outside of the VTA/SNc) labeled in each condition using the injection schematic shown in Figure 1H with the indicated injection sites of AAV-FLEX-TVA on the x-axis of the graph. Mean ± s.e.m.

Figure 3 – figure supplement 1: Distribution of projection-specific populations of dopamine neurons within the midbrain

A summary of the projection-specified populations of dopamine neurons labeled (using the injection scheme from Figure 1A) in cyan, compared to the distribution of all DAT-cre expressing neurons in the area of the injection in red. Distribution of: VS-projecting dopamine neurons, DS-projecting dopamine neurons**,** TS-projecting dopamine neurons**,** GP-projecting dopamine neurons**,** Amy-projecting dopamine neurons**,** OFC-projecting dopamine neurons**,** mPFC-projecting dopamine neurons**,** lHb-projecting dopamine neurons**,** and selected landmarks for reference **(A-D)**. Plots were prepared by projecting all neurons within 400 μm of the selected coronal plane onto a single image. Bars represent 2 mm.

Figure 3 – figure supplement 2: Distribution of projection-specific populations of dopamine neurons within the midbrain: Maximum Intensity Projection

For each graph, 75 neurons were sampled at random from 3 of the (-RG) brains shown in Figure 3 – figure supplement 1. These 225 neurons were then plotted as a "maximum intensity projection" (i.e. their Z coordinate was ignored). In the case of Lhb-projecting dopamine neurons, labeling was very sparse, so we plotted all 122 neurons. The distribution of all DAT-cre expressing neurons is shown in red. The distribution of dopamine neurons projecting to the indicated site in each case is shown in cyan. Grid lines indicate 500 microns.

Figure 3 – figure Supplement 3: Comparison of labeled cell distribution between control and experimental groups

A comparison of the distribution of labeled VTA/SN neurons in experiments lacking RG (labeling dopamine "starter neurons" only) and experiments with RG (labeling dopamine "starter neurons" as well as their monosynaptic inputs). Coronal planes match Figure 3 – figure supplement 1 B and C. VS, DS, and TS are color-coded, while the total distribution of all DAT-Cre expressing neurons in the area are shown in red.

Figure 3 – figure Supplement 4: Injection Sites

CLARITY-based brain clearing did not preserve native BFP fluorescence, so brains were physically sectioned and stained with an anti-BFP antibody to label the injection site of AAV-FLEX-TVA in each animal. All injection sites used for input tracing (based on the schematic in Figure 1G) are summarized in the left panels and a single raw image from each is displayed in the panels on the right. Injection sites were intended to allow TVA uptake into VS-projecting **(A-A')**, DS-projecting, **B-B')**, TS-projecting **(C-C')**, GP-projecting **(D-D')**, Amy-projecting **(E-E')**, OFC-projecting **(F-F')**, mPFC-projecting **(G-G')**, and lHb-projecting **(H-H')** dopamine neurons. Red: injection sites. Blue: autofluorescence.

Figure 3 – figure supplement 5: Subdivisions of the striatum

A) Maximum intensity projection (horizontal) of the outline of the brain (black), the dorsal striatum (green), the nucleus accumbens (orange), and the injections into VS (blue), DS (cyan), and TS (red). Stereotactic coordinates are shown as grid lines with 1mm spacing. **B)** Maximum intensity projection (sagittal) of the outline of same injection sites as shown in above. C) Coronal views of the approximate centers of the VS/DS and TS injections.

Figure 4 – figure supplement 1: Comparison of the percentage of inputs from selected regions across populations of projection-specific dopamine neurons

A summary of the distribution of inputs among the 20 most prominent regions providing input to dopamine neurons. These areas were selected based on the maximum percentage of inputs among 8 conditions for each area. Plots are identical to those displayed in Figure 4 and each condition is

labeled with the same color as in Figure 4. *p*-Values are given based on 1-way ANOVA. Asterisks (*) indicate significant differences among conditions after Holm-Sidak corrections for multiple comparisons.

Figure 7 – figure supplement 1: Density-based analysis of inputs to projection-specified dopamine neurons

All neurons from all animals were plotted in a reference space with 20μm x 20μm x 20μm voxels, and a 3D Gaussian with kernel size of 60μm x 60μm x 60μm was used to estimate density at each voxel. **A)** A typical optical coronal section of raw fluorescence containing the ventral striatum colored such that black indicates fluorescence. **B)** Average fluorescence among all animals displayed as a heat map. **C)**. Density estimate based on Gaussian smoothing of the image generated by plotting all extracted centroids from all animals displayed as a heat map. **D)** A series of coronal sections demonstrating the 3D structure of the patches, obtained by finding the local maxima from C and expanding stepwise pixel-by-pixel until either 1/3 maximum intensity or another patch boundary was reached. Patch coloring matches Figure 7. Bars represent 2 mm.

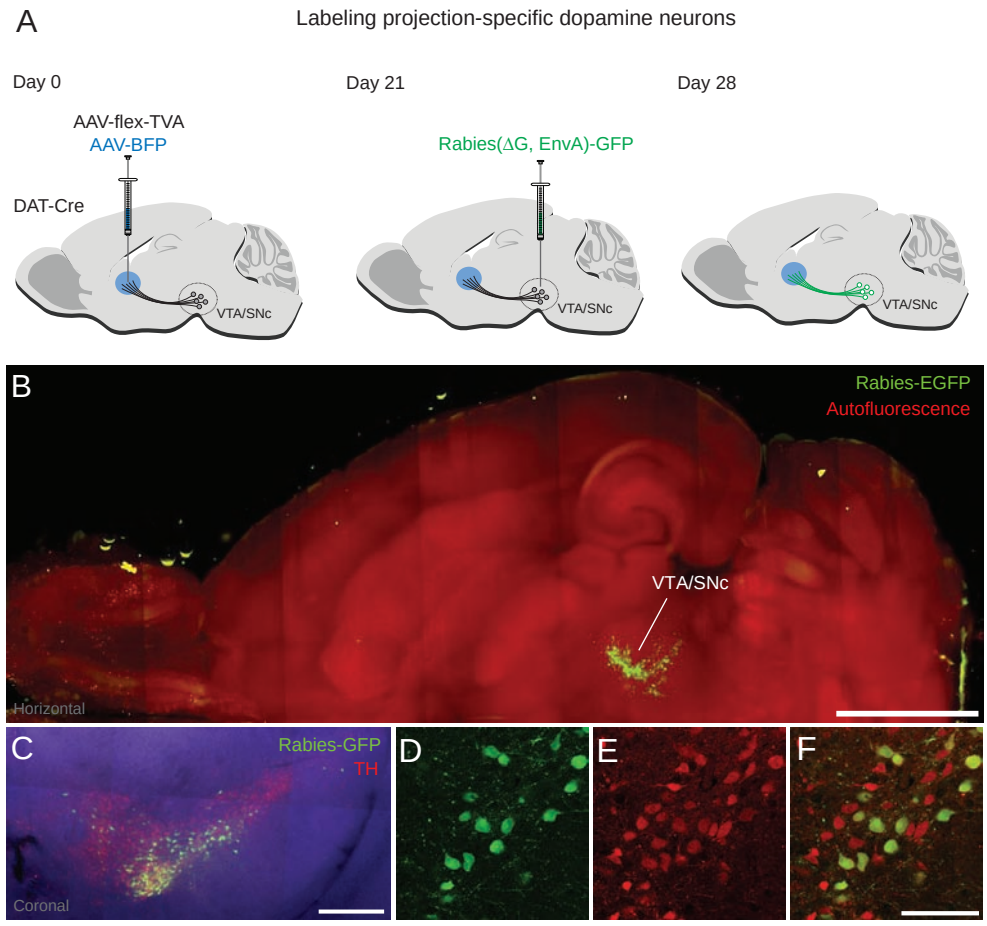
A
Labeling projection-specific dopamine neurons
Day 0
Day 21
Day 28
AAV-flex-TVA
AAV-BFP
DAT-Cre
VTA/SNc
Rabies(ΔG, EnvA)-GFP
VTA/SNc
VTA/SNc
B
Rabies-EGFP
Autofluorescence
VTA/SNc
Horizontal
C
Rabies-GFP
TH
Coronal
D
E
F

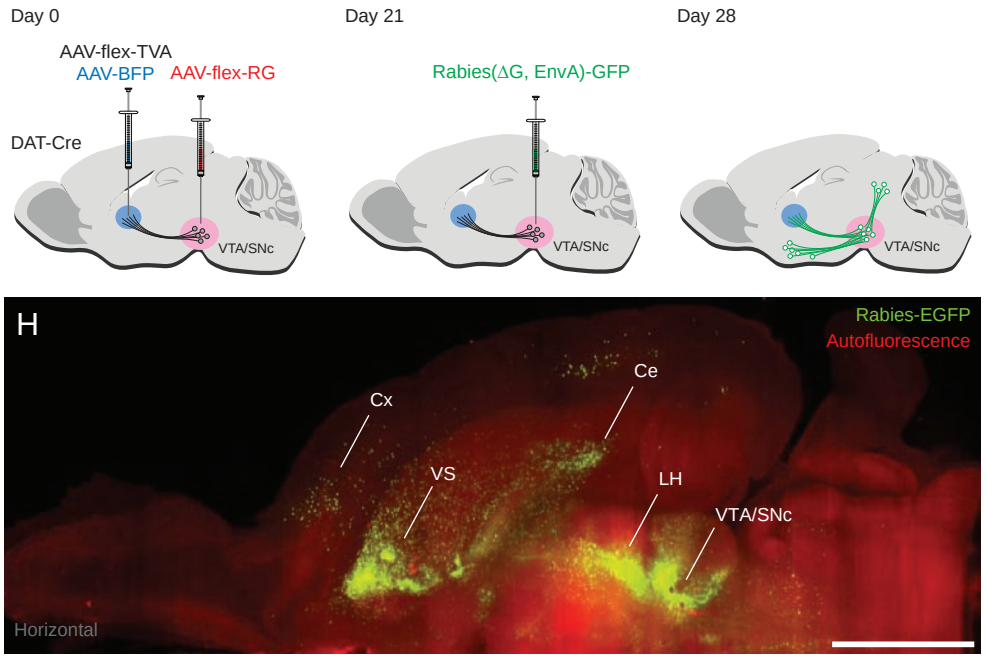
G
Labeling monosynaptic inputs to projection-specific dopamine neurons
Day 0
Day 21
Day 28
AAV-flex-TVA
AAV-BFP
AAV-flex-RG
DAT-Cre
VTA/SNc
Rabies(ΔG, EnvA)-GFP
VTA/SNc
VTA/SNc
H
Rabies-EGFP
Autofluorescence
Cx
Ce
VS
LH
VTA/SNc
Horizontal

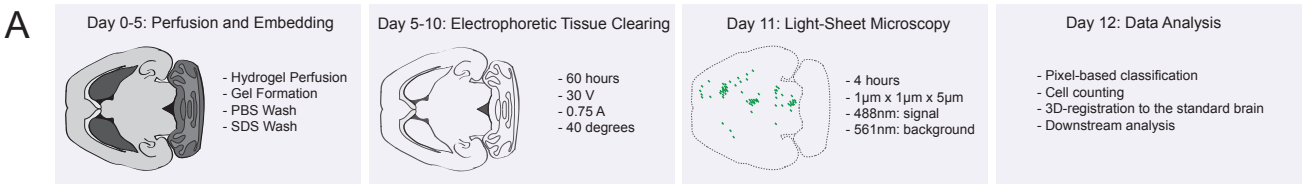
A
Day 0-5: Perfusion and Embedding
- Hydrogel Perfusion
- Gel Formation
- PBS Wash
- SDS Wash
Day 5-10: Electrophoretic Tissue Clearing
- 60 hours
- 30 V
- 0.75 A
- 40 degrees
Day 11: Light-Sheet Microscopy
- 4 hours
- 1µm x 1µm x 5µm
- 488nm: signal
- 561nm: background
Day 12: Data Analysis
- Pixel-based classification
- Cell counting
- 3D-registration to the standard brain
- Downstream analysis

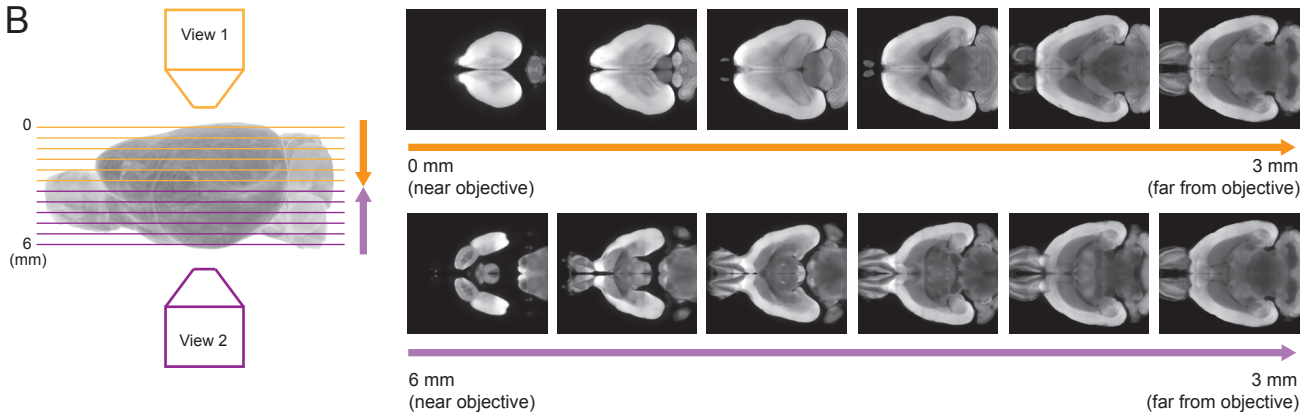
B
View 1
0
6
(mm)
View 2
0 mm
(near objective)
3 mm
(far from objective)
6 mm
(near objective)
3 mm
(far from objective)

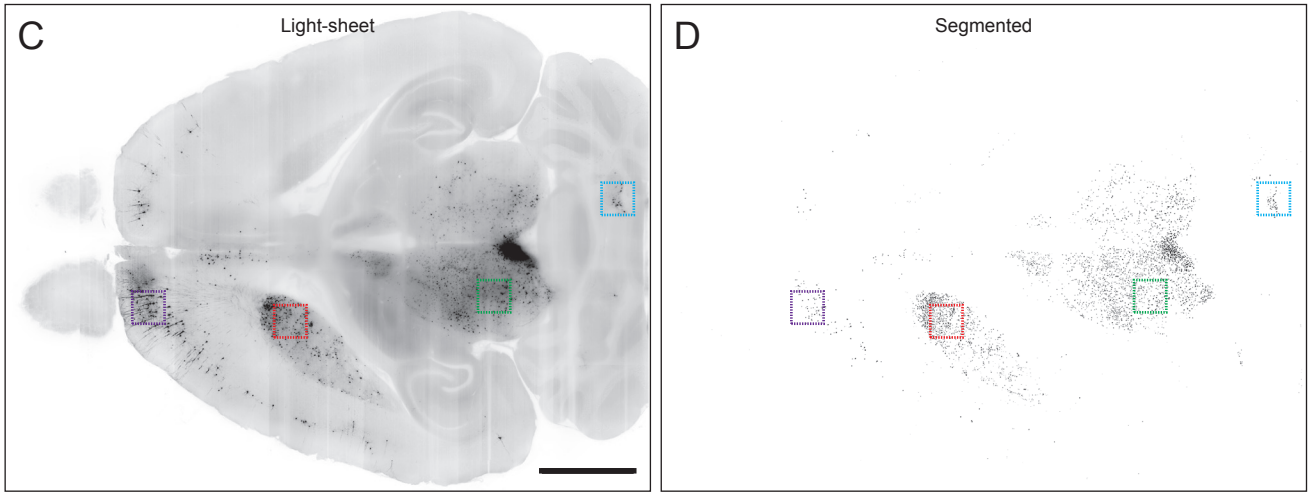
C
Light-sheet
D
Segmented

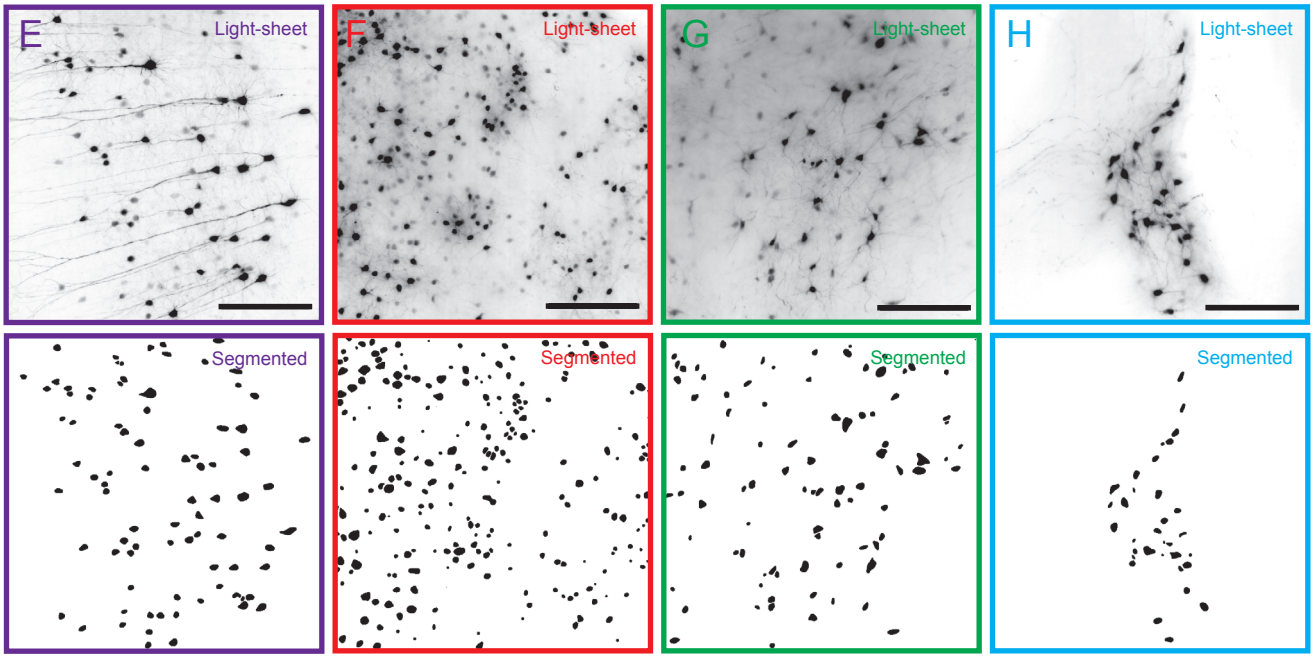
E
Light-sheet
F
Light-sheet
G
Light-sheet
H
Light-sheet
Segmented
Segmented
Segmented
Segmented

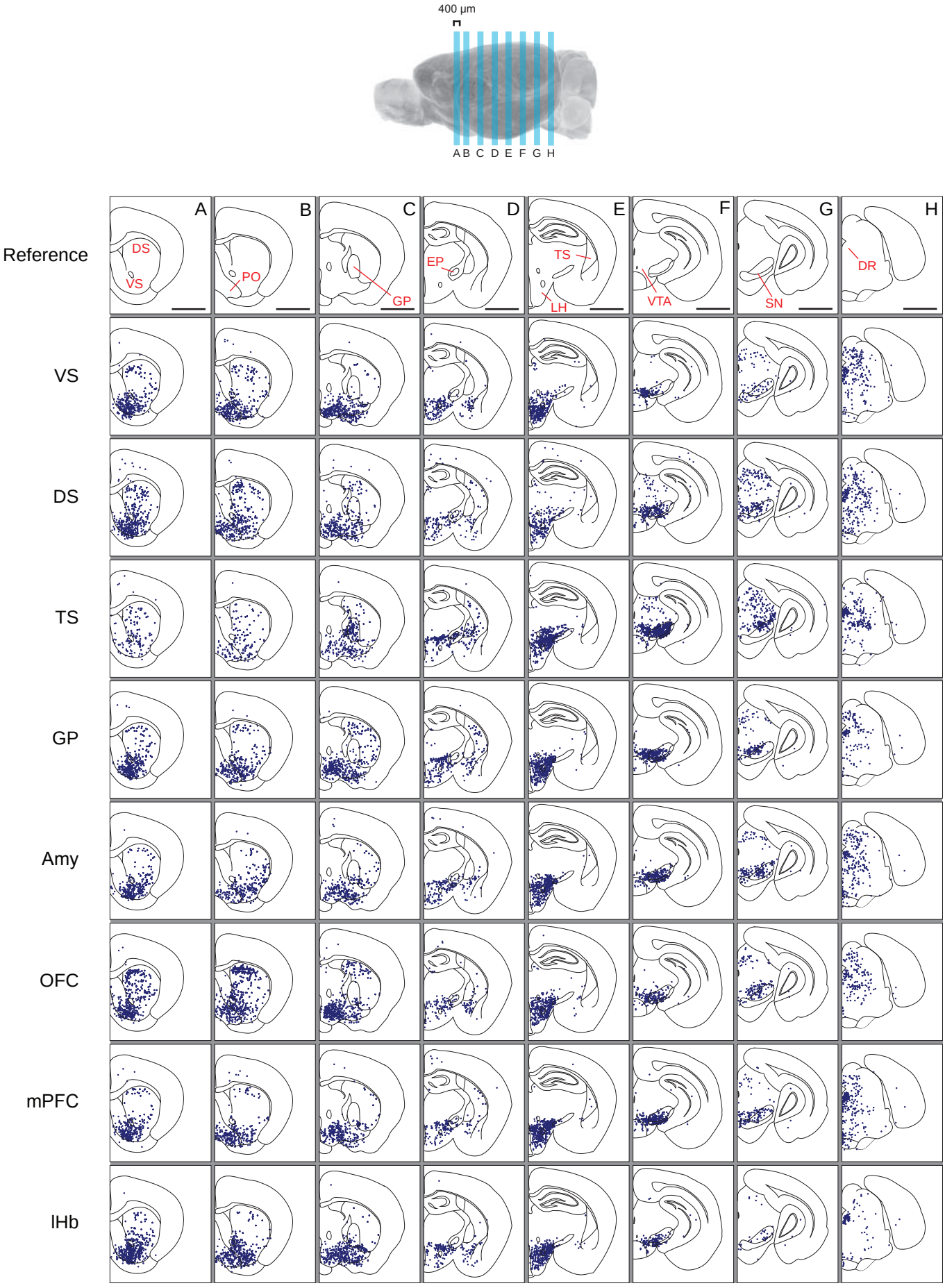
400 µm
A B C D E F G H
Reference
VS
DS
TS
GP
Amy
OFC
mPFC
lHb
A
B
C
D
E
F
G
H
DS
VS
PO
GP
EP
TS
LH
VTA
SN
DR

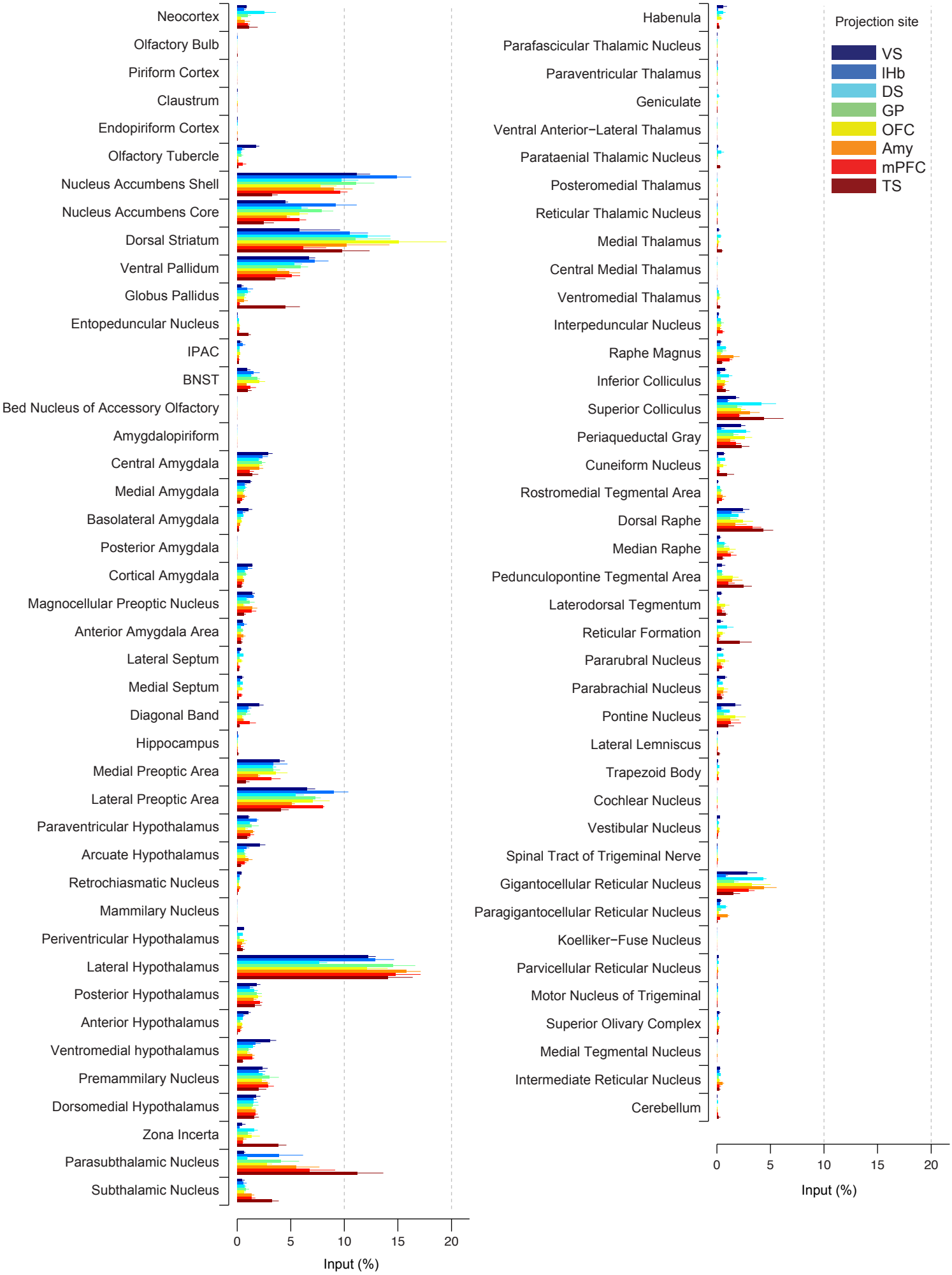
Neocortex
Olfactory Bulb
Piriform Cortex
Claustrum
Endopiriform Cortex
Olfactory Tubercle
Nucleus Accumbens Shell
Nucleus Accumbens Core
Dorsal Striatum
Ventral Pallidum
Globus Pallidus
Entopeduncular Nucleus
IPAC
BNST
Bed Nucleus of Accessory Olfactory
Amygdalopiriform
Central Amygdala
Medial Amygdala
Basolateral Amygdala
Posterior Amygdala
Cortical Amygdala
Magnocellular Preoptic Nucleus
Anterior Amygdala Area
Lateral Septum
Medial Septum
Diagonal Band
Hippocampus
Medial Preoptic Area
Lateral Preoptic Area
Paraventricular Hypothalamus
Arcuate Hypothalamus
Retrochiasmatic Nucleus
Mammilary Nucleus
Periventricular Hypothalamus
Lateral Hypothalamus
Posterior Hypothalamus
Anterior Hypothalamus
Ventromedial hypothalamus
Premammilary Nucleus
Dorsomedial Hypothalamus
Zona Incerta
Parasubthalamic Nucleus
Subthalamic Nucleus
0
5
10
15
20
Input (%)
Habenula
Parafascicular Thalamic Nucleus
Paraventricular Thalamus
Geniculate
Ventral Anterior−Lateral Thalamus
Parataenial Thalamic Nucleus
Posteromedial Thalamus
Reticular Thalamic Nucleus
Medial Thalamus
Central Medial Thalamus
Ventromedial Thalamus
Interpeduncular Nucleus
Raphe Magnus
Inferior Colliculus
Superior Colliculus
Periaqueductal Gray
Cuneiform Nucleus
Rostromedial Tegmental Area
Dorsal Raphe
Median Raphe
Pedunculopontine Tegmental Area
Laterodorsal Tegmentum
Reticular Formation
Pararubral Nucleus
Parabrachial Nucleus
Pontine Nucleus
Lateral Lemniscus
Trapezoid Body
Cochlear Nucleus
Vestibular Nucleus
Spinal Tract of Trigeminal Nerve
Gigantocellular Reticular Nucleus
Paragigantocellular Reticular Nucleus
Koelliker−Fuse Nucleus
Parvicellular Reticular Nucleus
Motor Nucleus of Trigeminal
Superior Olivary Complex
Medial Tegmental Nucleus
Intermediate Reticular Nucleus
Cerebellum
0
5
10
15
20
Input (%)
Projection site
VS
lHb
DS
GP
OFC
Amy
mPFC
TS

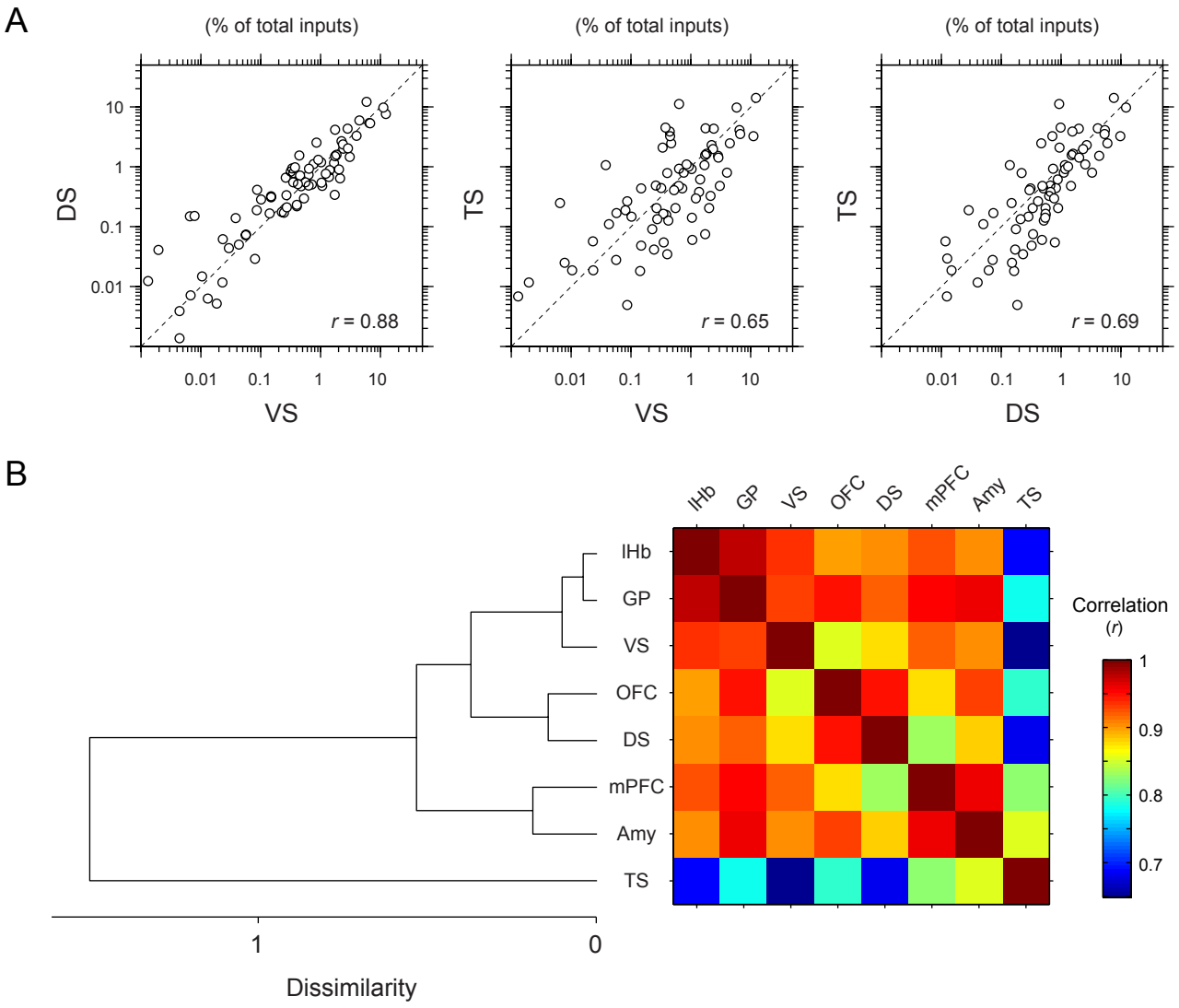
A
(% of total inputs)
DS
VS
r = 0.88
(% of total inputs)
TS
VS
r = 0.65
(% of total inputs)
TS
DS
r = 0.69
0.01
0.1
1
10
B
lHb
GP
VS
OFC
DS
mPFC
Amy
TS
Correlation
(r)
1
0.9
0.8
0.7
1
0
Dissimilarity

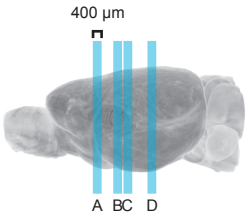
400 µm
A BC D

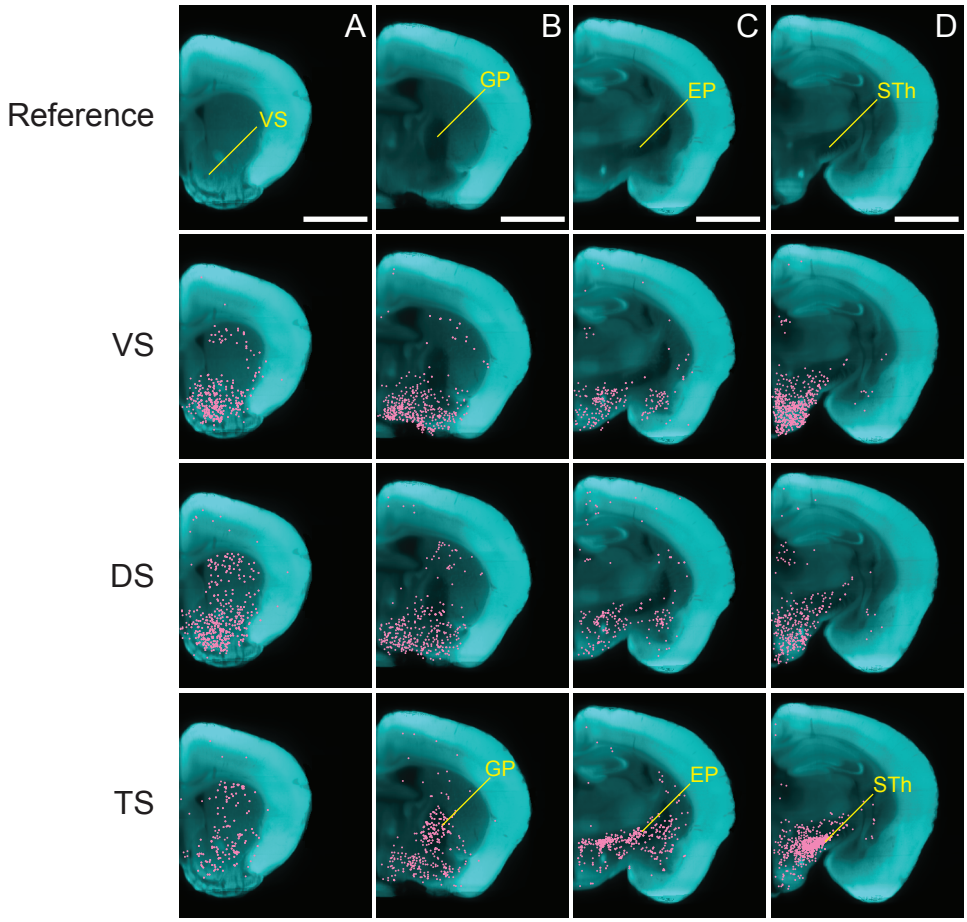
Reference
VS
DS
TS
A
B
C
D
VS
GP
EP
STh
GP
EP
STh

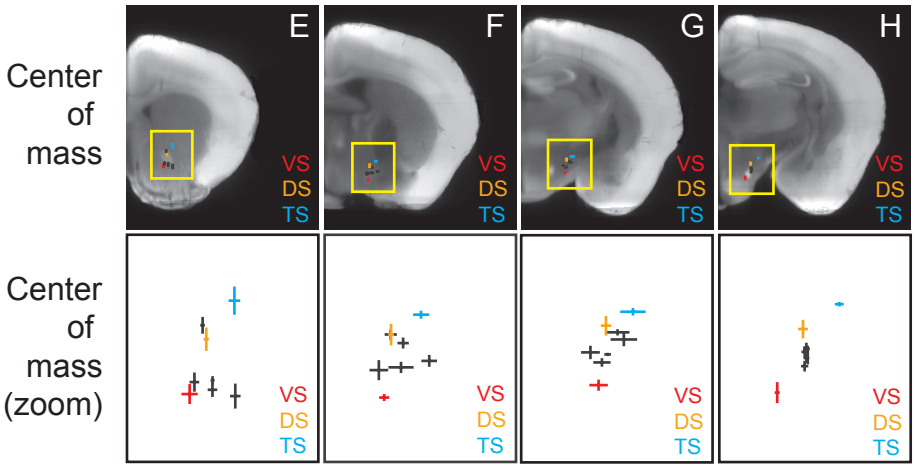
Center of mass
Center of mass (zoom)
E
F
G
H
VS
DS
TS

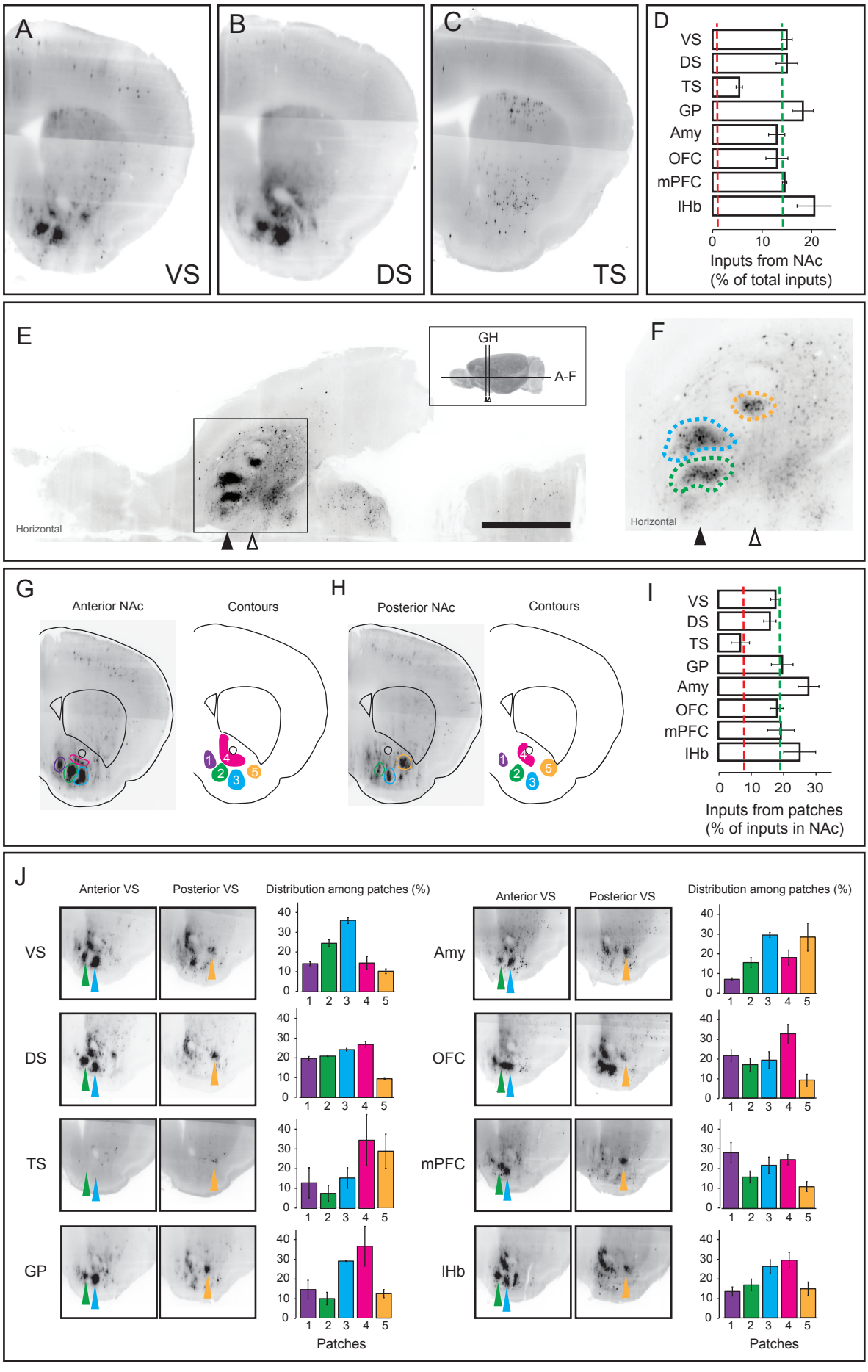
A
VS
B
DS
C
TS
D
VS
DS
TS
GP
Amy
OFC
mPFC
lHb
0
10
20
Inputs from NAc
(% of total inputs)
E
GH
A-F
Horizontal
F
Horizontal
G
Anterior NAc
Contours
H
Posterior NAc
Contours
I
VS
DS
TS
GP
Amy
OFC
mPFC
lHb
0
10
20
30
Inputs from patches
(% of inputs in NAc)
J
Anterior VS
Posterior VS
Distribution among patches (%)
VS
DS
TS
GP
Amy
OFC
mPFC
lHb
0
10
20
30
40
1
2
3
4
5
Patches

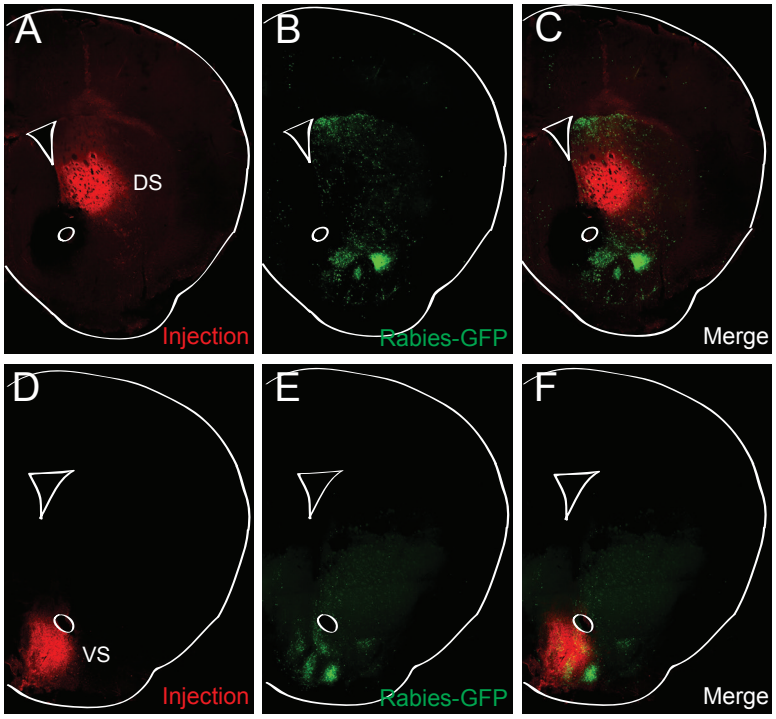
A
DS
Injection
B
Rabies-GFP
C
Merge
D
VS
Injection
E
Rabies-GFP
F
Merge

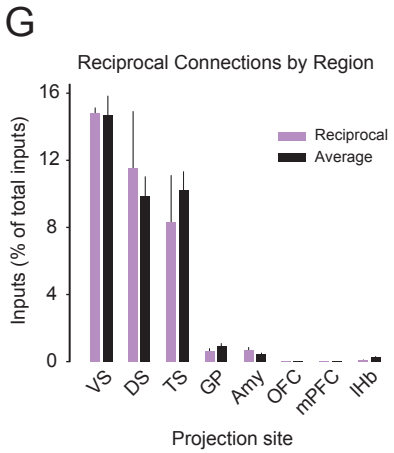
G
Reciprocal Connections by Region
Inputs (% of total inputs)
16
12
8
4
0
Reciprocal
Average
VS
DS
TS
GP
Amy
OFC
mPFC
lHb
Projection site

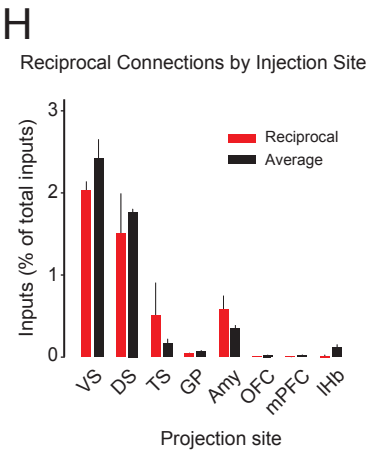
H
Reciprocal Connections by Injection Site
Inputs (% of total inputs)
3
2
1
0
Reciprocal
Average
VS
DS
TS
GP
Amy
OFC
mPFC
lHb
Projection site

A. Parallel model

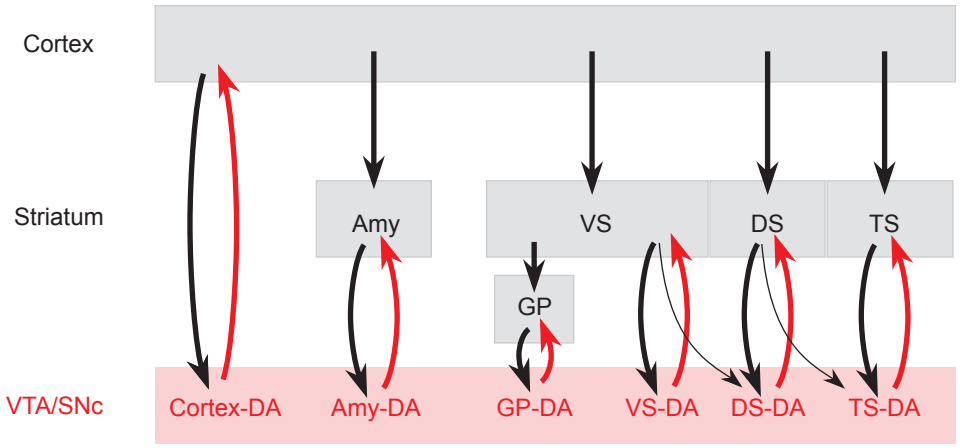

B. New model